博士論文

Identification of NEK9 as a selective autophagy adaptor to regulate ciliogenesis

(一次繊毛形成を制御する選択的オートファジーアダプター NEK9 の同定)

山本　康博

Identification of NEK9 as a selective autophagy adaptor to regulate ciliogenesis

Affiliation: Department of Respiratory Medicine, Graduate School of Medicine,

The University of Tokyo, Tokyo 113-0033, Japan

Supervisor: Takahide Nagase

Yasuhiro Yamamoto

Contents

Pages

Abbreviations

ARL13B: ADP Ribosylation Factor Like GTPase 13B

ATG: Autophagy related gene

CRISPR: clustered regularly interspaced short palindromic repeat

cDNA: complementary deoxyribonucleic acid

DAPI: 4',6-diamidino-2-phenylindole

EDTA: ethylenediaminetetraacetic acid

FIP200: Focal adhesion kinase (FAK) family interacting protein 200

GABARAP: Gamma-aminobutyric acid receptor-associated protein

GFP: green fluorescent protein

gRNA: guide RNA

HEK293T: Human Embryonic Kidney cells 293T

HK-2: Human kidney 2

HRP: horseradish peroxidase

IBAQ: Intensity Based Absolute Quantification

IFT20: Intraflagellar transport 20

KO: knock out

LAMP1: Lysosomal-associated membrane protein 1

LC3: Microtubule-associated protein light chain 3

LTL-FITC: Lotus Tetragonolobus Lectin-fluorescein

MYH9: Myosin heavy chain 9

NBR1: Neighbor of BRCA1 gene 1

NCBI: National Center for Biotechnology Information

NDP52: Nuclear domain 10 protein 52

OPTN: Optineurin

PAM: protospacer adjacent motif

PCR: polymerase chain reaction

PVDF: polyvinylidene difluoride

RNA: ribonucleic acid

siRNA: small interfering RNA

SDS-PAGE: sodium dodecyl sulfate-poly-acrylamide gel electrophoresis

SEM: standard error of the mean

TAX1BP1: Tax1-binding protein 1

WIPI: WD repeat domain, phosphoinositide interacting

Abstract

Autophagy regulates primary cilia formation, but the underlying mechanism is not fully understood. Here, I identified NIMA-related kinase 9 (NEK9) as a GABARAPs-interacting protein and found that NEK9 and its LC3-interacting region (LIR) are required for primary cilia formation. Mutation in the LIR of NEK9 in mice also impaired *in vivo* cilia formation in the kidneys. Mechanistically, NEK9 interacts with MYH9 (also known as myosin IIA), which was implicated in inhibiting ciliogenesis through stabilization of the actin network. MYH9 accumulates in NEK9 LIR mutant cells and mice, and depletion of MYH9 restored ciliogenesis in NEK9 LIR mutant cells. These results suggest that NEK9 regulates ciliogenesis by acting as an autophagy adaptor for MYH9. Given that the LIR in NEK9 is conserved only in land vertebrates, the acquisition of the autophagic regulation of the NEK9–MYH9 axis is likely a novel mechanism regulating ciliogenesis with possible adaptive implications for terrestrial life.

Keywords:

Selective autophagy, primary cilia

Introduction

The primary cilium is a highly dynamic microtubule-based organelle that protrudes from the plasma membrane when cells exit the cell cycle [1]. It extends from the basal body that matures from the mother centriole of the centrosome (Figure 1). Primary cilia sense and transduce various extracellular stimuli, such as signaling molecules (*e.g.*, Hedgehog, Wnt, Notch, growth factors, and hormones), mechanical forces (*e.g.*, fluid flow and tissue deformation), and environmental cues (*e.g.*, light and odorants), depending on the cell type [2-4]. They regulate diverse developmental and physiological processes, such as embryonic patterning, organogenesis, tissue homeostasis, and cell differentiation [2,5,6]. Accordingly, defects in ciliogenesis lead to a collection of genetic syndromes known as ciliopathies, which have characteristic features that include renal, hepatic, and pancreatic cysts, skeletal anomalies, retinal degeneration, hearing loss, obesity, brain malformations, and mental retardation [7,8].

Macroautophagy (hereafter autophagy) is an intracellular degradation process in which cytoplasmic material is degraded in the lysosome. During autophagy, a fraction of the cytoplasm is sequestered by small membrane cisternae called isolation membranes (or phagophores) to form autophagosomes [9,10]. Autophagosomes then

fuse with lysosomes to degrade their engulfed material (Figure 2). Autophagy degrades cytoplasmic contents nonselectively or selectively [11,12] (Figure 3). Selective autophagy cargos include certain soluble proteins, protein aggregates, organelles, including mitochondria, the endoplasmic reticulum (ER), and lysosomes, and intracellular pathogens [13-16]. Selective autophagy is important for maintaining cellular homeostasis and has been implicated in human diseases [17,18]. In mammals, selective autophagy cargos are recognized by ATG8 proteins, which are classified into two subfamilies, namely, the LC3 (including LC3A, LC3B, and LC3C) and GABARAP (including GABARAP, GABARAPL1, and GABARAPL2) subfamilies. They are covalently conjugated to phosphatidylethanolamine in the autophagic membrane and bind to selective cargos with a LC3-interacting region (LIR) motif [19,20]. Alternatively, some LIR-containing soluble proteins, such as SQSTM1 (p62), NBR1, NDP52, OPTN, and TAX1BP1, work as selective autophagy adaptors to mediate binding between ATG8s and cargos [11,12].

Recent evidence suggests that autophagy regulates primary cilia formation bilaterally; cilia regulate autophagy induction, whereas autophagy regulates ciliogenesis [21,22]. Centriolar satellites are non-membranous organelles in the vicinity of the centrosome, which act as conduits for centrosomal components and regulate

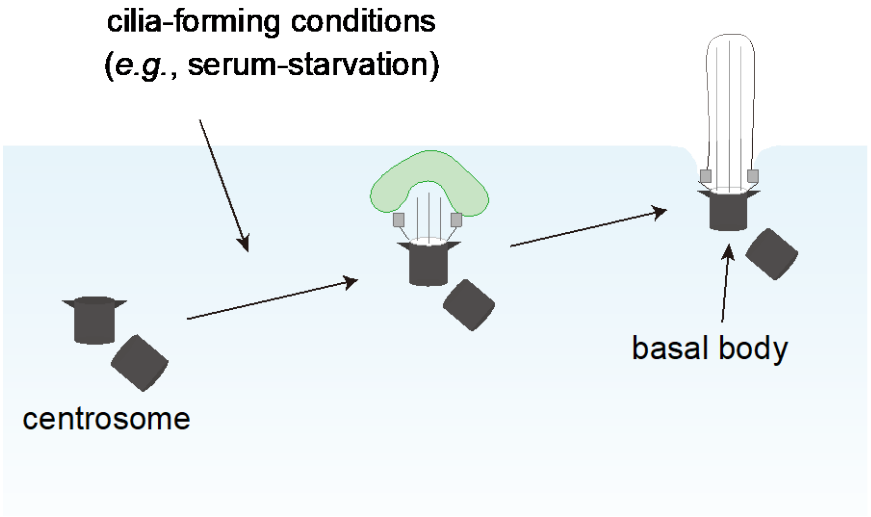

Figure 1. Primary cilium forms from the basal body

Primary cilium protrudes from the plasma membrane when cells exit the cell cycle. It extends from the basal body that matures from the mother centriole of the centrosome.

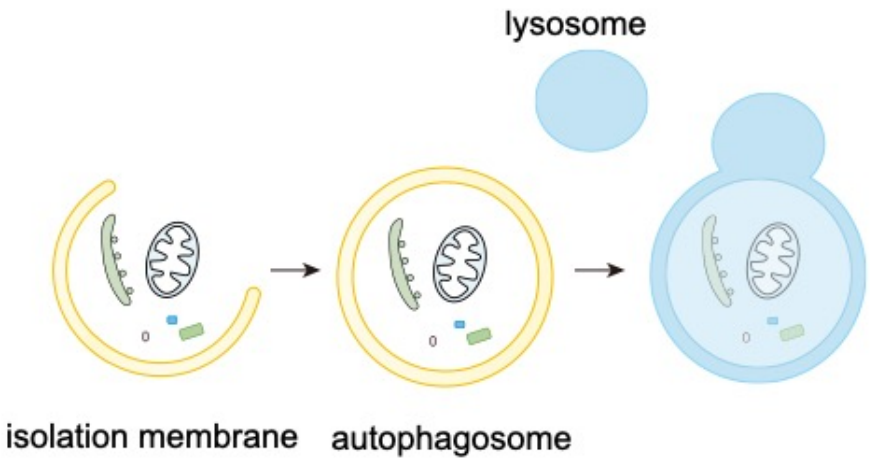

Figure 2. Scheme of autophagy

During autophagy, a fraction of the cytoplasm is sequestered by small membrane cisternae called isolation membranes (or phagophores) to form autophagosomes. Autophagosomes then fuse with lysosomes to degrade their engulfed material.

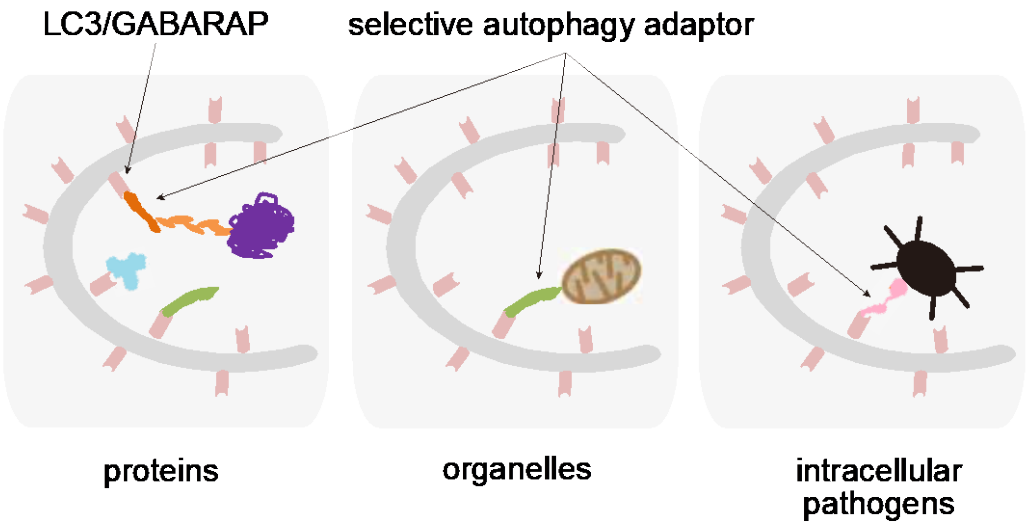

Figure 3. Scheme of selective autophagy

Selective autophagy degrades certain soluble proteins, protein aggregates, organelles, and intracellular pathogens. Selective autophagy cargos are recognized by LC3/GABARAP covalently conjugated to phosphatidylethanolamine in the autophagic membrane. LC3/GABARAP bind to selective cargos with a LC3-interacting region (LIR) motif. Some LIR-containing soluble proteins work as selective autophagy adaptors to mediate binding between LC3/GABARAP and cargos.

ciliogenesis and ciliary functions [23,24]. Centriolar oral-facial-digital syndrome 1 (OFD1) is essential for ciliogenesis; it promotes the docking of the basal body to the plasma membrane and recruits essential ciliary components to the basal body [25,26]. By contrast, OFD1 at centriolar satellites acts as a suppressor of ciliogenesis by blocking recruitment of Bardet–Biedl syndrome 4 (BBS4), a crucial component for cilia elongation. Autophagy degrades OFD1 at centriolar satellites but not at centrioles, thus promoting ciliogenesis [27]. Upregulation of autophagy consistently promotes ciliogenesis in cells across various culture conditions [27-31]. Primary cilia formation is impaired in autophagy-deficient *Atg7-KO* kidney proximal tubular cells in mice, but the underlying mechanisms remain undetermined [30]. By contrast, other reports have shown that basal autophagy can negatively regulate ciliogenesis [32,33]. Under nutrient-rich conditions, basal autophagy degrades IFT20, a protein essential for ciliogenesis, thus preventing unwanted ciliogenesis during cell proliferation [32]. This complicated relationship between autophagy and cilia may indicate the existence of an unidentified key regulator [21].

Here, I describe the identification of NIMA-related kinase 9 (NEK9) as a GABARAPs-interacting protein. This GABARAP–NEK9 interaction was found to be important for primary cilia formation in culture cells and mice. NEK9 functions as a

selective autophagy adaptor for MYH9 (also known as Myosin IIA), a negative regulator of ciliogenesis. NEK9-mediated autophagic degradation of MYH9 facilitates actin remodeling and induces ciliogenesis by increasing actin dynamics. I also show that autophagy promotes ciliogenesis primarily by degrading NEK9–MYH9 and OFD1.

Materials and Methods

Cell lines

Mouse embryonic fibroblasts (MEFs), HeLa cells, and HEK293T cells were cultured in Dulbecco's modified Eagle's medium (DMEM) (D6546; Sigma-Aldrich) supplemented with heat-inactivated 10% fetal bovine serum (FBS; 173012; Sigma-Aldrich) and 2 mM L-glutamine (25030-081; GIBCO) in a 5% CO_2 incubator. HK-2 cells were cultured in DMEM/F-12 (Dulbecco's modified Eagle's Medium Nutrient Mixture F-12; 11320033; GIBCO) medium supplemented with 10% FBS, 1% ITS (insulin, transferrin and sodium selenite media supplement, I1884; Sigma-Aldrich), and 2 mM L-glutamine. For the starvation treatment, cells were washed twice with phosphate-buffered saline (PBS) and incubated in amino acid-free DMEM (048-33575; Wako Pure Chemical Industries) without serum. For the serum-starvation treatment, cells were washed twice with PBS and incubated in DMEM supplemented with 2 mM L-glutamine. *Fip200*-KO [74] and *Atg3*-KO [75] MEFs have been described previously. To generate stable cell lines, cells were cultured with retrovirus or lentivirus, and stable transformants were selected with puromycin (P8833; Sigma-Aldrich), blasticidin (022-18713; Wako Pure Chemical Industries), or geneticin (10131035; Thermo Fisher Scientific).

Mouse strains

All animal experiments were approved by the Institutional Animal Care and Use Committee of the University of Tokyo (Medical-P17-084) and the Animal Care and Use Committee of the National Institute of Quantum and Radiological Science and Technology (1610111 and 1610121). Wild-type C57BL/6 mice were obtained from Japan SLC, Inc. *Atg5*$^{-/-}$*;NSE-Atg5* mice have been previously described [50].

Generation of *Nek9*$^{W967A/W967A}$ mice

Nek9$^{W967A/W967A}$ mice were generated by CRISPR-mediated knockin of the W967A mutation at the mouse *Nek9* genomic locus. Oocyte/embryo manipulation was performed as previously described [76]. Briefly, MII oocytes were collected from superovulated C57BL/6J females and fertilized *in vitro*. The fertilized one-cell embryos were washed with Opti-MEM I (Life Technologies) and transferred into a 1-mm electroporation cuvette (CUY501P1-1.5; Nepa Gene Co.) containing 5 μL of a mixture of recombinant Cas9 protein (50 ng/μL, Nippon Gene), gRNA (0.8 μM, Alt-R CRISPR-Cas9 System; Integrated DNA Technologies), and ssODN (0.5 μg/μL, PAGE Ultramer DNA Oligo; Integrated DNA Technologies) in Opti-MEM I. The sequence of the gRNA targeting exon 22 of mouse *Nek9* was 5′-TCGGAGTCCTGGTGCCTCCT-3′. The sequence of the

donor oligonucleotide (ssODN) was 5′-TCCTGAGGGCTATGTGGGCTCAGGAGACTAGAGGCTGGGTCGACAAGAGTCTGTTCCGAGGAGGCAGGCGGACTCCGAGTCTAAGTCAGGCTTTGGATCCATTTCCATTTCTTCCTTTGCTGTCTGGGT-3′. Electroporation was conducted using a NEPA21 Super Electroporator (Nepa Gene Co.) under the following conditions: four poring pulses at 40 V, with a pulse width of 3.5 ms and pulse interval of 50 ms; five transfer pulses at 7 V, with a pulse width of 50 ms and pulse interval of 50 ms. After electroporation, the embryos were immediately recovered from the cuvette, washed with Opti-MEM I, and cultured overnight in KSOM medium. The embryos that developed normally to the two-cell stage were transferred to the oviduct of pseudopregnant ICR females (CLEA Japan, Inc.) on the day of the vaginal plug (Day 0.5). Genomic DNA of offspring (F0 founders) was collected by tail biopsy and used for genotyping. F0 founders harboring potential mutant alleles were bred to wild-type C57BL/6J mice, and mutations in the F1 generation were confirmed by sequencing. Genotyping was performed by PCR using primers flanking the target site (forward primer, 5′-CAGCCAGTTCACTTTTCATACTACATCCCCCAAATG-3′; reverse primer, 5′-CAAAGCCAGGTCCACAGGACCCTTCCATTCTCCCA-3′).

Plasmids

cDNAs encoding human NEK9 (NP_001316166.1), MYH9 (NP_002464.1), OFD1 (NP_001317138.1), GABARAP (NP_009209), GABARAPL1 (NP_113600), LC3B (NP_073729), Actin (NP_001092.1) were inserted into pMRX-vector [77]. DNAs encoding enhanced GFP, codon-optimized mRuby3 (modified from pKanCMV-mClover3-mRuby3; 74252; Addgene) [78], and 3×FLAG were also used for tagging. Mutated or truncated constructs were prepared by PCR-mediated site-directed mutagenesis. Single-guide RNAs (sgRNAs) targeting exon 2 of mouse *Nek9* (5′-CACCACCCTGCTGATTGAGC-3′, 5′-GCTGATTGAGCTGGAGTACT-3′), exon 22 of mouse *Nek9* (5′-TCGGAGTCCTGGTGCCTCCT-3′) and exon 22 of human *NEK9* (5′-TACAGGAGTCTGTTCCCAGG-3′) were cloned into pSpCas9(BB)-2AGFP (a gift from Dr. F. Zhang, Broad Institute of Massachusetts Institute of Technology; Addgene #48138). For generation of *Nek9*^{W967A} MEFs and *NEK9*^{W967A} HK-2 cells, donor plasmids harboring short homology arms (800 bps each, with one arm covering exon 22 of mouse *Nek9* or human *NEK9,* which includes the bases encoding the LIRs) were generated from the pCMV vector. The homology arms were amplified by PCR and inserted between the *Bam*HI and *Hind*III sites of the pCMV vector. The primer sequences were 5′-GGATCCGAAGGGAGGGAAGAGTCATTCCTTGGCTCTG-3′,

5′-GGATCCTTTCCTGAGGGCTATGTGGGCTCAGGAGACT-3′,5′-AAGCTTCTGGGACCCAAAGAACTTCACCGCACACTTAC-3′, and 5′-AAGCTTCTGAAGCTTCAAACATCCACGGTGAAAGCAAC-3′ for *Nek9*^{W967A} MEFs and 5′-GGATCCCATTAAACATTTTTAGTGAAAATACTTCAAAG-3′, 5′-GGATCCCTAGAGGCTGGGTCTACAGGAGTCTGTTCC-3′, 5′-AAGCTTTCTCCTGAGCCTGTAGAGCCCCCAGGAGACT-3′, and 5′-AAGCTTCTAGACATTCAGAAAGAAAGTGGTTGGGGCTG-3′ for *NEK9*^{W967A} HK-2 cells. A neomycin-resistance gene was inserted into the PstI site of the pCMV vector. The W967A mutation in NEK9 was introduced by PCR-mediated site-directed mutagenesis.

Antibodies and reagents

The following antibodies were used for immunoblotting: mouse monoclonal antibody against HSP90 (610419; BD) and rabbit polyclonal antibodies against NEK9 (A301-139A; Bethyl), NEK8 (A0984; ABclonal), NEK7 (3057S; Cell Signaling), MYH9 (A0173; ABclonal), MYH10 (A12029; ABclonal), OFD1 (NBP1-89355; Novus Biologicals), GABARAP (13733S; Cell Signaling Technology), p62/SQSTM1 (PM045; MBL), GFP (A6455; Thermo Fisher Scientific), and FLAG (F7425; Sigma-Aldrich).

Rabbit polyclonal antibody against LC3 was described previously [79]. HRP-conjugated anti-mouse and anti-rabbit IgG (111-035-003, 111-035-144; Jackson ImmunoResearch Laboratories) antibodies were used as secondary antibodies. The following antibodies were used for immunocytochemistry and immunohistochemistry: rabbit polyclonal antibodies against FIP200 (17250-1-AP; ProteinTech), WIPI2 (SAB4200400; Sigma-Aldrich), LAMP1 (ab24170; Abcam), NEK9 (A301-139A; Bethyl), OFD1 (NBP1-89355; Novus Biologicals), and pericentrin (abcam; 4448) and mouse monoclonal antibodies against LC3 (CTB-LC3-2-IC; CosmoBio) and ARL13B (abcam; 136648). Alexa Fluor 488-conjugated goat anti-mouse IgG, Alexa Fluor 568-conjugated goat anti-rabbit IgG, and Alexa Fluor 660-conjugated goat anti-mouse IgG (A-11029, A-11036, and A-21055; Thermo Fisher Scientific) were used as secondary antibodies. Hoechst 33342 (H342; Dojindo Molecular Technologies) or DAPI-containing SlowFade Antifade Mountant (S36938; Thermo Fisher Scientific) was used to stain DNA. LTL-FITC (Vector Laboratories; FL-1321-2) was used to stain proximal tubular cells. For transient expression, Fugene HD (VPE2311; Promega) was used. For bafilomycin A_1 treatment, cells were cultured with 100 nM bafilomycin A_1 (B1793; Sigma-Aldrich).

Preparation of lentivirus and retrovirus

To prepare the lentivirus, HEK293T cells were transiently transfected with a lentiviral vector together with pCMV-VSV-G (a gift from Dr. R. A. Weinberg, Whitehead Institute for Biomedical Research) and psPAX2 (a gift from Dr. D. Trono, Ecole Polytechnique Federale de Lausanne) using Lipofectamine 2000 (11668019; Thermo Fisher Scientific). After cells were cultured for 2–3 days, the supernatant was collected and passed through a 0.45-mm syringe filter unit (SLHV033RB; EMD Millipore). To prepare the retrovirus, HEK293T cells were transiently transfected with a retroviral vector together with pCG-VSV-G and pCG-gag-pol (a gift from Dr. T. Yasui, National Institutes of Biomedical Innovation, Health and Nutrition) using Lipofectamine 2000, and viral particles were collected from the supernatant as described above.

Establishment of *Nek9-KO* MEFs

Wild-type MEFs were transfected with pSpCas9(BB)-2AGFP encoding sgRNAs targeting exon 2 of mouse *Nek9*. Two days after transfection, GFP-positive cells were isolated using a cell sorter (MoFlo Astrios EQ; Beckman Coulter), and single clones were obtained. Clones with mutations in both alleles were identified by immunoblotting and sequencing of genomic DNA.

Establishment of *Nek9*^{W967A} MEFs and *NEK9*^{W967A} HK-2 cells

To generate *Nek9*^{W967A} MEFs, wild-type MEFs were co-transfected with pSpCas9(BB)-2AGFP encoding the sgRNA targeting exon 22 of mouse *Nek9* and the donor plasmid described above. Two days after transfection, GFP-positive cells were isolated using a cell sorter. After geneticin selection, single clones were obtained by the limiting dilution method. Clones harboring the W967A mutation and the neomycin-resistant cassette in both alleles were identified by PCR (forward primer, 5′-CTTTCACCCCTAACGTGAGTTTGGACTTCTTACTTTGTG-3′; reverse primer, 5′-CTGAAGCTTCAAACATCCACGGTGAAAGCAACCTGAGC-3′) and sequencing of genomic DNA. *NEK9*^{W967A} HK-2 clones were similarly generated and identified by PCR (forward primer, 5′-ATAGACACCTTGTATGGTTCTTTGGAGGATTAAATGAACT-3′; reverse primer, 5′-AAGAAAGTGGTTGGGGCTGCTGATATCAAGATCAGAACC-3′) and sequencing of genomic DNA.

siRNA-mediated knockdown

Stealth RNAi oligonucleotides were obtained from Thermo Fisher Scientific. The following sequences were used: siNEK9#1, 5′-AAUAGCAGCUGUGUGAGUCUUG-

3′; siNEK9#2, 5′-GCAGCCAAACUUUGAUUAAAGUU-3′; siNEK9#3, 5′-GCUGCCUUGGGAAUUCAGUACCA-3′; and siLuciferase (siLuc), 5-AAUUAAGUCCGCUUCUAAGGUUUCC-3′. The stealth RNAi oligonucleotides were transfected into cells using Lipofectamine RNAiMAX (13778150; Thermo Fisher Scientific) according to the manufacturer's instructions. Cells were harvested three days after transfection.

shRNA-mediated knockdown

pLKO.1-blast vectors (a gift from Keith Mostov; Addgene plasmid # 26655) respectively containing shRNAs to *Myh9* (sh#1, 5′- CCATACAACAAATACCGCTT-3′; sh#2, 5′-GGTAAATTCATTCGTATCAA-3′) and *Ofd1* (sh#1, 5′-GCTAGAATCTTTAGAGACAAA-3′; sh#2, 5′-TCACAAGAAGTCACGTAATAT-3′) as well as a non-targeting control (shScramble, 5′-CAACAAGATGAAGAGCACCAA-3′) were packaged into the lentivirus as described above. Cells were infected with the lentivirus, and stable transformants were selected with blasticidin. The knockdown efficiency was measured by immunoblotting.

Immunofluorescence

Cells grown on coverslips were washed with PBS and fixed in 4% paraformaldehyde (PFA; 09154-85; Nacalai Tesque) for 10 min at room temperature or in 100% methanol (21914-03;Nacalai Tesque) for 5 min at −30°C. The PFA-fixed cells were permeabilized with 50 mg/mL digitonin (D141; Sigma-Aldrich) in PBS for 5 min, blocked with 3% bovine serum albumin (BSA; 011-27055; Wako Pure Chemical Industries) in PBS for 30 min, and then incubated with primary antibodies for 1 h at room temperature or overnight at 4°C (for anti-OFD1 antibody). After washing three times with PBS, cells were incubated with Alexa Fluor 488/568/660-conjugated goat anti-mouse or anti-rabbit IgG secondary antibodies for 1 h at room temperature. Fluorescence microscopy was performed using a confocal laser microscope (FV1000 IX81; Olympus) with a 100 × oil-immersion objective lens (1.40 NA; Olympus) and captured with FluoView software (Olympus). The number of punctate structures and the colocalization rate were determined using Fiji software (ImageJ). For primary cilia quantification, cells were incubated to confluency and serum-starved for 24 h before fixation, and immunofluorescence images were obtained in 15 serial z-stack series at 0.4-μm intervals. The percentage of cells with cilia was measured by dividing the number of cilia (ARL13B-positive structures) by the number of nuclei (DAPI). Cilia length was determined by the Pythagorean theorem method [80].

Histology and immunohistochemistry

For hematoxylin and eosin staining, mouse tissues were fixed in 4% PFA overnight at 4°C, and infiltrated with 15% and then 30% sucrose in PBS for 4 h each. Tissues were then embedded in Tissue-Tek OCT Compound (Sakura Japan Co.) and frozen at −80°C. Sections (7 μm) were prepared using a cryostat (CM3050 S, Leica Microsystems) and mounted on slides. Cryosections were stained with hematoxylin and eosin and photographed using a microscope (BX51; Olympus) equipped with a digital camera (DP70; Olympus). For immunohistochemistry, mouse tissues were frozen after fixation in Tissue-Tek OCT Compound and cryosections were prepared. Cryosections were permeabilized with 50 mg/mL digitonin in PBS for 5 min, blocked with 3% BSA in PBS for 30 min, and incubated with primary antibodies in 3% BSA for 1 h, followed by a PBS wash and incubation for 1 h with secondary antibodies.

Immunoprecipitation and immunoblotting

Cells were lysed in a lysis buffer (50 mM Tris-HCl, pH 7.5, 150 mM NaCl, 1 mM EDTA, 1% Triton X-100, PhosSTOP [4906837001; Roche], and complete EDTA-free protease inhibitor [03969-21;Nacalai Tesque]). After centrifugation at 17,700 × *g* for 10 min, the supernatants were incubated with anti-FLAG M2 affinity gel (A2220; Sigma-Aldrich) for 3 h at 4°C with gentle rotation. Precipitated immunocomplexes were washed three times in washing buffer (50 mM Tris-HCl, pH 7.5, 150 mM NaCl, 1 mM EDTA, and 1% Triton X-100) and boiled in sample buffer (46.7 mM Tris- HCl, pH 6.8, 5% glycerol, 1.67% sodium dodecyl sulfate, 1.55% dithiothreitol, and 0.02% bromophenol blue). Samples were subsequently separated by sodium dodecyl sulfate polyacrylamide gel electrophoresis and transferred to Immobilon-P polyvinylidene difluoride membranes (IPVH00010; EMD Millipore). Immunoblotting analysis was performed with the indicated antibodies. Super-Signal West Pico Chemiluminescent Substrate (1856135; Thermo Fisher Scientific) or Immobilon Western Chemiluminescent HRP Substrate (P90715; EMD Millipore) was used to visualize the signals, which were detected using the Fusion Solo 7S system (M&S Instruments). Appropriate contrast and brightness adjustment and quantification were performed using Fiji software (ImageJ).

Liquid chromatography-tandem mass spectrometry (LC-MS/MS) analysis of GABARAPL1 and GABARAPL1$^{Y49A/N50A}$ immunoprecipitates

FLAG-GABARAPL1 and FLAG-GABARAPL1$^{Y49A/N50A}$ plasmids were prepared as described above. FLAG-GABARAPL1 and FLAG-GABARAPL1$^{Y49A/N50A}$-interacting proteins were immunoprecipitated from HEK293T cells and identified by LC-MS/MS analysis using a high-performance LabDroid system at Robotic Biology Institute (https://rbi.co.jp/en/). All MS/MS spectra were searched against protein sequences of the NCBI nonredundant human protein dataset (NCBInr RefSeq Release 71, containing 179,460 entries) using the Protein Pilot software package (Sciex). Protein quantification was performed using the iBAQ method [81] without conversion to absolute amounts by using universal proteomics standards (iBQ). The iBQ value was calculated by dividing the sum of the ion intensities of all the identified peptides of each protein by the number of theoretically measurable peptides.

LC-MS/MS analysis of FLAG-NEK9 immunoprecipitates

MEFs stably expressing FLAG or FLAG-NEK9 were incubated to confluency, serum-starved for 24 h, and lysed with lysis buffer (50 mM Tris-HCl, pH 7.5, 150 mM NaCl, 1% NP-40, and complete EDTA-free protease inhibitor [03969-21; Nacalai Tesque]).

After centrifugation at 17,700 × *g* for 10 min, the supernatants were incubated with anti-FLAG M2 magnetic beads for 3 h at 4°C with gentle rotation. The eluted proteins were enzymatically digested according to a phase-transfer surfactant (PTS) protocol [82]. Then, 50-µL eluted samples were mixed with 85 µL of PTS buffer. Samples were reduced with 10 mM dithiothreitol at room temperature for 30 min and alkylated with 50 mM 2-iodoacetamide (804744; Sigma-Aldrich) at room temperature for 30 min. Next, samples were diluted five-fold by adding 50 mM NH_4HCO_3 solution followed by digestion with 1 µg of Lysyl Endopeptidase (LysC; 121-05063; Wako Pure Chemical Industries) at 37°C for 4 h. Samples were further digested with 1 µg of trypsin at 37°C for 8 h. An equal volume of ethyl acetate acidified with 0.5% TFA was added to the digested samples. After centrifugation at 10,000 × *g* for 10 min twice at room temperature, the aqueous phase containing peptides was collected and dried using a SpeedVac concentrator (Thermo Fisher Scientific). The dried peptides were solubilized in 100 µL of 2% acetonitrile and 0.1% TFA, and the peptide mixture was trapped on a hand-made C18 STAGE tip prepared as previously reported [83]. The trapped peptides were subjected to a previously reported dimethyl-labeling procedure [84]. Subsequently, $^{13}CH_2O$ and $NaBH_3CN$ (light label) were added to the FLAG-only sample. Similarly, $^{13}CD_2O$ and $NaBD_3CN$ (heavy label) were added to the FLAG-NEK9 sample. The dimethyl-labeled peptides left on the

tip were eluted with 100 μL of 80% acetonitrile and 0.1% TFA. The light/heavy-labeled eluents were mixed and dried using a SpeedVac concentrator. The sample was dissolved in 2% acetonitrile and 0.1% TFA and loaded onto the LC-MS system with a Q-Exactive MS instrument (Thermo Fisher Scientific) equipped with a nano HPLC system (Advance UHPLC; Bruker Daltonics) and an HTC-PAL autosampler (CTC Analytics) with a trap column (0.3 x 5 mm, L-column, ODS, Chemicals Evaluation and Research Institute). Samples were separated by a gradient using mobile phases A (0.1% formic acid/H_2O) and B (0.1% formic acid and 100% acetonitrile) at a flow rate of 300 nL/min (4% to 32% B for 190 min, 32% to 95% B for 1 min, 95% B for 2 min, 95% to 4% B for 1 min, and 4% B for 6 min) with a home-made capillary column (length of 200 mm and inner diameter of 100 μm) packed with 2-μm C18 resin (L-column2, Chemicals Evaluation and Research Institute). Then, the eluted peptides were electrosprayed (1.8–2.3 kV) and introduced into the MS equipment (positive ion mode, data-dependent MS/MS). The obtained raw data were subjected to database search (UniProt, reviewed mouse database as of September 13th, 2018) with Sequest HT algorithm running on Proteome Discoverer 2.2 (Thermo Fisher Scientific). The parameters for database searches were as follows: peptide cleavage was set to trypsin; missed cleavage sites were allowed to be up to two residues; peptide lengths were set to 6–144 amino acids; and mass tolerances were set to 10 ppm for

precursor ions and 0.02 Da for fragment ions. For modification conditions, carbamidomethylation at cysteine and dimethylation [H(4)C(2), or H(-2)D(6)^{13}C(2)] at lysin and peptide N-terminus were set as fixed modifications. Oxidation at methionine was set as a variable modification. A significance threshold of $p < 0.05$ was applied. Abundances of precursor ions were calculated based on the area of the precursors with Proteome Discoverer 2.2.

Fluorescence recovery after photobleaching

MEFs expressing GFP-actin were incubated to confluency and serum-starved for 24 h before analysis. Fluorescence microscopy was performed using a confocal laser microscope (FV3000; Olympus) with a 100 × oil-immersion objective lens (1.40 NA; Olympus) and captured with FluoView software (Olympus). The chamber was maintained at 37°C and continuously supplied with humidified 5% CO_2. Five pre-bleaching images were acquired at 5-s intervals, and circular regions of interest (ROI) with radii of 2 μm were selected and bleached with an 80% power 488-nm laser for 800 ms. Fluorescence recovery was recorded for 250 s by acquiring images at 5 s intervals. Pre- and post-bleach images were taken with 0.5% power. Fluorescence intensity was analyzed by Fiji and its simFRAP plug-in (https://imagej.nih.gov/ij/plugins/sim-

frap/index.html). Briefly, the mean intensity values of the ROIs, total image, and background fluorescence were calculated. After background subtraction, the mean intensity values of ROIs were normalized with those of each total image for each time-point.

Multiple sequence alignment and sequence analysis

Amino acid sequences of each protein were obtained from the NCBI protein database and aligned using the ClustalW algorithm in MEGA 10.0 [85]. The disordered regions were predicted using the PSIPRED protein sequence analysis workbench (http://bioinf.cs.ucl.ac.uk/psipred/). The LIR was predicted using iLIR search (https://ilir.warwick.ac.uk/).

Statistical analysis

Statistical analysis was performed using GraphPad Prism 8 software (GraphPad software). The statistical methods used for each analysis are specified in the figure legends.

Results

Differential interactome screen identified NEK9 as a GABARAPs-interacting protein.

To identify substrates or adaptors of selective autophagy, a differential interactome screen using wild-type GABARAPL1 and the LIR-docking site mutant GABARAPL1$^{Y49A/L50A}$ was performed by my collaborator Dr. Chino (Figure 4A). The immunoprecipitates were subjected to mass spectrometry, and 3129 proteins were detected (Table 1), including known GABARAP- and LC3-interacting proteins such as p62/SQSTM1, TEX264, and PCM1 [12,34,35]. Based on binding intensity and specificity to wild-type GABARAPL1, I selected four candidate proteins NEK9, TSR2, ACSM3, NUCB2 for further screen (Figure 4B). Among them, I focused on NEK9, because it was less characterized in the context of autophagy, and the other three proteins did not interact with GABARAPL1 in subsequent immunoprecipitation analysis (Figure 4C). NEK9 was also previously identified as a protein interacting with ATG8 family proteins [36].

NEK9 belongs to the NEK family, which is associated mainly with cell-cycle-related functions during mitosis [37,38]. NEK9 is activated during mitosis and

phosphorylates various downstream substrates to facilitate proper mitosis progression [39-42]. Homozygous *Nek9* knockout mice are embryonic lethal (MGI: 2387995).

Some NEK family proteins, such as NEK1, NEK8, and NEK10, have cilia-related functions besides mitotic regulation and are causative genes of human ciliopathies [43-45]. A study of one pedigree indicated that a recessive loss-of-function mutation in *NEK9* (a missense mutation in the middle region) causes a lethal skeletal dysplasia (lethal congenital contracture syndrome 10; OMIM 609798), and patient fibroblasts showed a defect in primary cilia formation [46]. *NEK8*, a close homolog of *NEK9*, is also a gene responsible for ciliopathy [44]. Very recently, it was reported that NEK9 has a LIR and suppresses selective autophagy by phosphorylating Thr50 within the LIR-docking site of LC3B [47]. However, how NEK9 is involved in primary cilia formation and whether its function relates to autophagy remain unknown.

NEK9 consists of an N-terminal kinase domain, followed by autoinhibitory regulator of chromosome condensation 1 (RCC1)-repeats and a coiled-coil domain (Figure 5) [39]. NEK9 has intrinsically disordered regions (residues 750–891 and 940–979) in the C-terminal region. NEK9 interacted with the GABARAP subfamily, but also with the LC3 subfamily to a lesser extent (Figure 6). The iLIR search predicted the presence of a LIR (WCLL) in the C-terminal disordered region (Figure 5) [48].

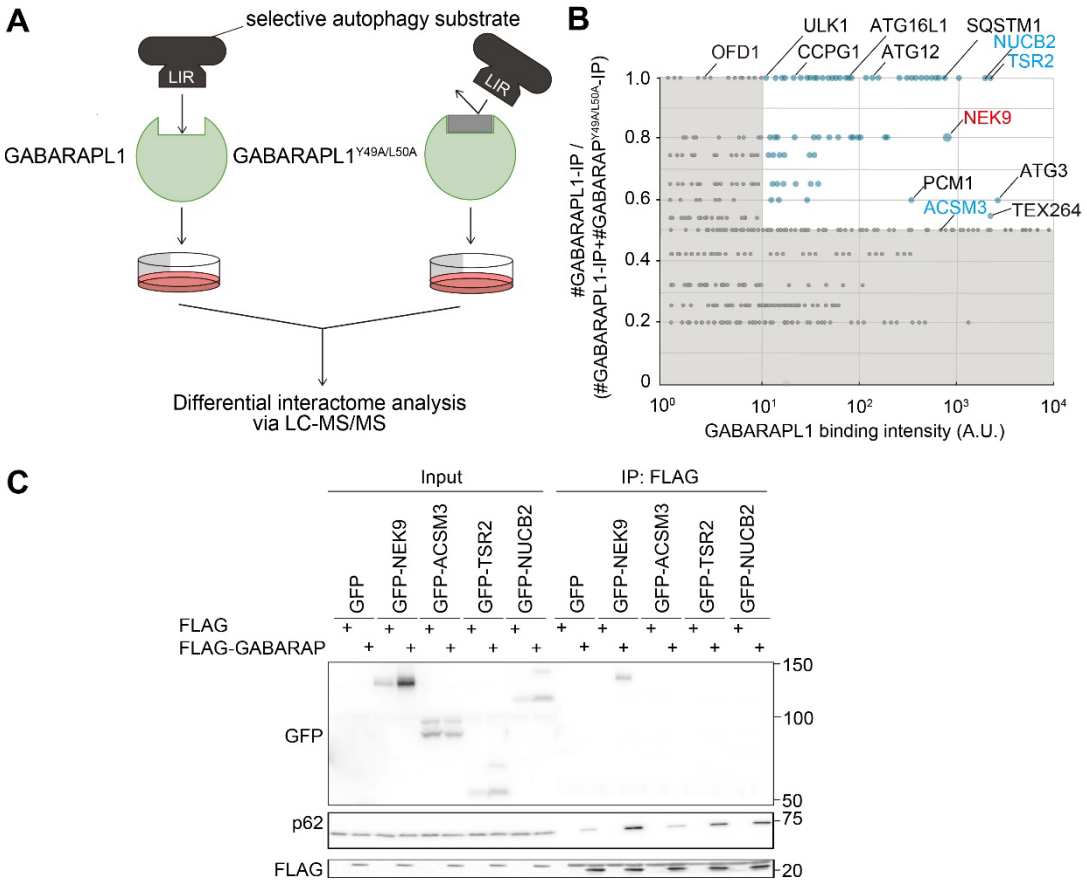

Figure 4. Differential interactome screen identified NEK9 as a GABARAPs-interacting protein

(A) Scheme of the differential interactome screen to identify substrates or adaptors of selective autophagy using GABARAPL1 and its LIR docking site mutant GABARAPL1$^{Y49A/N50A}$.

(B) Results of the differential interactome screen. Four independent immunoprecipitation and mass spectrometry (MS) analyses were conducted. The number of times each protein was detected is shown as #GABARAPL1-IP or #GABARAPL1$^{Y49A/N50A}$-IP. The *x*- and *y*-axes represent GABARAPL1 binding intensity and the #GABARAPL1-IP / (#GABARAPL1-IP + #GABARAPL1 $^{Y49A/N50A}$ -IP) ratio, respectively. The area defined by $x < 10$ or $y < 0.5$ is colored gray. Proteins which were subjected to secondary screening are shown in blue.

(C) Co-immunoprecipitation of FLAG-GABARAP and GFP-tagged candidate proteins. Data are representative of three independent experiments.

Table 1. The results of the differential interactome screen using GABARAPL1 (wild-type) and its LIR docking site mutant GABARAPL1$^{Y49A/N50A}$ (mutant).

Four independent immunoprecipitation and mass spectrometry (MS) were performed by my collaborator Dr. Chino. Top 150 proteins with high binding intensity are listed. The binding intensity (arbitrary unit) and the number of times each protein was detected are shown. Proteins which were subjected to secondary screening are shown in blue.

	intensity（mean）			the number of times	
	control	wild-type	mutant	control	wild-type
proteinid					
GABARAPL1		205012.9642	128021.3	0	4
GABARAP		116417.0498	80753.91	0	4
EIF5A	105430.5028	93080.71704	79163.87	4	4
EIF5AL1	67045.11745	39361.24669	34784.16	4	4
EIF5A2	27810.87738	20172.01335	24830.01	4	4
NONO	17138.1474	17319.53769	16517.57	4	4
IGKV2-26	2892.219511	11179.95182	8404.901	4	4
EEF1A1	6748.287924	10239.83984	20848.18	4	4
ATG4B		7191.082662	67.93504	0	4
PRSS1	6905.590166	7189.999361	5657.164	4	4
WDR77	10861.46944	7051.358567	7321.5	4	4
MIF	8738.473606	6875.219906	3212.74	4	4
MDH2	5496.750569	6621.279919	6218.352	4	4
SFN	5383.367387	5803.758078	4802.201	4	4
PRMT5	8370.315148	5534.814916	4809.028	4	4
TUBA1A	4025.443377	5358.316743	4109.979	4	4
ATG3		5258.875118	86.09757	0	4
UBL5	4423.428602	4748.665344	3759.345	4	4
RPS27A	1983.496938	4396.864613	2341.735	4	4
TEX264		4219.262882	36.94718	0	4
SFPQ	3738.130211	4002.376146	4166.315	4	4

SFPQ	5503.469228	3323.7557	3683.702	4	3
TCP1	3877.625746	3286.405298	3067.463	4	4
CCT8	3953.655752	3252.820416	2695.53	4	4
C11orf84	4152.6249	3220.930528	2767.521	4	4
PPIA	4368.735655	3108.64746	1595.988	4	4
TXN	3123.390169	2990.502336	2202.563	4	4
STK38	3070.312596	2821.508939	2874.114	4	4
HSPA1A	2073.438642	2771.370005	2015.403	4	4
CCT3	3147.434445	2730.592965	2678.376	4	4
HSPA8	2369.910022	2658.654003	2615.374	4	4
HSP90	2361.185567	2650.935838	2810.88	4	4
CCT7	2900.774947	2634.654125	2198.667	4	4
B-ALPHA-1	2289.072532	2618.205421	1863.116	4	4
DNAJC5G		2607.31931		0	1
CCT6A	2762.066246	2601.079131	2070.861	4	4
C1QBP	2123.292481	2519.010606	2265.667	4	4
PFN1	2635.122271	2379.413719	1112.839	4	4
RRRRRETFRF1	1813.643	2361.1455		1	2
LRPAP1	2414.92013	2346.948401	1768.968	4	4
SUMO2	2426.794509	2230.135138	1258.093	4	3
ATP5B	2071.947043	2050.173541	2011.387	4	4
RPLP2	634.6407953	2048.67933	1766.807	4	4
EEF1A1	1943.401567	2040.163574	5402.149	4	4
CALU	186.8249077	1968.31839	210.349	4	4
NUDT21	1802.982115	1956.977288	26732.89	4	4
HNRNPK	2108.231519	1945.691923	1724.689	4	4
ATP5A1	1668.685627	1868.968496	1911.206	4	4
IPO5	129.3030115	1844.653413	129.9659	4	4
TUBB	1969.091338	1842.07216	2258.258	4	4
LDHB	2366.441366	1807.316744	1294.917	4	4
HSP90AB1	1657.823033	1766.690035	1945.164	4	4
DDX42	1627.984842	1765.721076	1613.972	4	4
CKB	1754.271139	1732.901642	926.5369	4	4
PPIB	1572.644056	1695.17444	1508.115	4	4
PSPC1	1721.639905	1679.57905	1732.583	4	4
IGK		1661.710349	1499.804	0	3
PSMA4	1559.903884	1654.810353	1651.417	4	4

TSR2		1644.40399		0	4
STK38L	2030.87704	1625.503998	1692.613	4	4
B-ALPHA-1	1769.982884	1605.773884	1534.101	4	4
RBM3	1417.26322	1588.23363	1002.236	4	4
HSP90AA1	1807.055941	1580.503524	1975.43	4	4
ACTA1	1982.348535	1576.692592	1197.159	4	4
PRDX2	1927.8128	1558.85131	1315.874	4	4
SLC25A31	649.4894214	1550.752077	1702.653	4	4
CSNK1D	696.7240861	1537.48785	1014.218	4	4
TUBB	904.4819744	1468.255324	912.5815	4	4
AAMDC	1399.572478	1455.107579	1091.46	4	4
PRSS1	1266.330037	1435.849451	1968.898	1	4
SPIN1	1972.324492	1427.273565	1378.87	4	4
YWHAE	1472.043444	1426.979391	965.1288	4	4
NME1	1366.932579	1422.781715	524.6661	4	4
EEF2	1705.119863	1404.275463	995.5837	4	4
ACTA1	1764.082883	1393.412173	1000.66	4	4
TUBA1B	1440.920102	1361.922135	1481.365	4	4
IGKV2-29	284.1954238	1315.014695		1	1
TUBB4B	1063.553213	1302.42976	1267.202	4	4
HSP90AA1	1040.149573	1295.786746	1405.75	4	4
VCP	1069.146016	1261.036628	1255.649	4	4
TUBB	1040.684241	1229.484839	1506.768	4	4
STK38	1136.659021	1205.605319	1155	4	4
HSPA8	1064.914217	1205.268854	1264.163	4	4
RPS28	1085.305236	1197.216668	772.1823	4	4
RPS26	65.29935663	1185.933305	86.09996	2	3
TUBB	672.8996902	1171.63638	1146.001	4	4
HSPA1A	930.7423715	1156.562588	1000.796	4	4
PHGDH	1149.493554	1146.877461	1333.927	4	4
NUCB2	6.156615854	1140.147287		1	4
CNRIP1	960.0118444	1132.138994	1034.184	4	4
PPIA	1472.088599	1122.827366	636.2768	4	4
SLC25A5	884.6001789	1111.446267	1290.017	4	4
NSMAF		1096.715774		0	4
YWHAB	1006.993129	1091.853475	914.0355	2	3
SLC25A5	658.8420094	1082.995903	1102.117	4	4

PRPS1	894.9651429	793.9411692	694.0551	4	4
TBCA	11.42556452	786.5201419		1	2
EEF1G	710.383776	784.2680909	14030.52	4	4
SOD1	1133.889707	781.9543202	338.6703	4	4
HMGB2	895.9275654	780.1491122	557.5821	4	4
SLC25A4	429.2910618	778.1943294	741.0553	4	4
RAN	737.3310882	775.3365662	426.9744	2	2
SNRPF	725.0732778	772.0116944	831.8186	4	4
ACSM3		766.4838947	31.23606	0	1
PRKAR1A	5.82180678	756.9321462	35.58525	3	4
ACTB|ACTG1	926.0508827	754.8198347	373.3854	4	4
GLOD4	791.6538259	754.6431035	580.3737	4	4
NEK9	7.953148775	752.39862	5.692064	4	4
HSPA1A	513.1514221	744.859131	681.6467	3	2
KPNB1	688.9438561	741.9360111	836.3159	4	4
GSTP1	911.5885396	735.2246094	361.7949	4	4
PPIA	933.2550096	726.9484279	458.7478	4	4
PPM1B	765.4033308	725.974065	455.335	4	4
YWHAZ	775.3051004	715.1190214	515.8421	4	4
CA2	1125.721718	707.867352	415.3126	4	4
IGKV2-29		697.98072	521.9011	0	2
PAICS	543.6341351	694.4428392	667.222	4	4
CALM2	490.0160306	688.177875	537.4619	4	2
POU3F1	673.3001249	688.0439908		1	1
LANCL2	672.2568988	684.6303733	687.216	4	4
RCN2	89.29603804	680.8951065	114.5883	2	4
TUBB3		679.0767609	759.4629	0	1
RPSA	691.8219907	659.0313488	400.1165	4	4
RAN	740.1430941	647.3471537	399.0651	4	4
HSP90AB1	590.8278169	646.7694119	659.0896	4	4
HMGB1	642.2778878	646.1449667	361.0906	4	4
HSD17B10	474.9919242	637.8442403	484.7531	4	4
HSP90AA1	493.039243	633.8967261	641.9777	4	4
PRPF38A	38.12091844	627.1205598	65.26042	4	4
RPS3	412.1287534	624.1823846	544.54	4	4
TRIR	507.6972267	621.6887328	619.9357	4	4
DHX15	560.5187163	619.7777289	519.7541	4	4

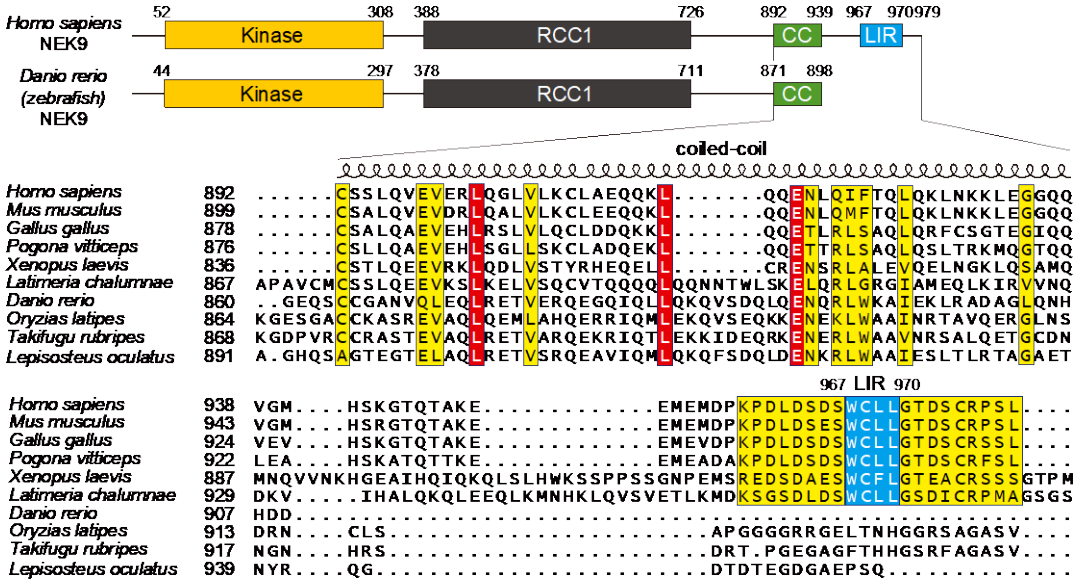

Figure 5. LIR in NEK9 is present only in land-living vertebrates

Structures of *Homo sapiens* and *Danio rerio* NEK9 and a multiple sequence alignment of NEK9 proteins in vertebrates. Although the overall structure of NEK9 is conserved among all vertebrates, the LIR is present only in land-living vertebrates, including mammals, reptiles, birds, and amphibians, but not in fish. The LIR is conserved in the coelacanth (*Latimeria chalumnae*), an extant species of ancestral lobe-finned fish from which terrestrial vertebrates evolved. Identical and similar residues are colored in red and yellow, respectively. LIR was predicted by iLIR search. KD, kinase-domain; RCC1, RCC1-repeats; CC, coiled-coil.

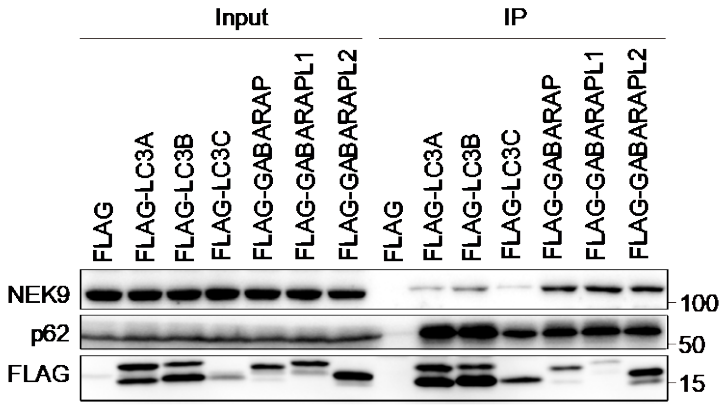

Figure 6. NEK9 interacts with LC3 and GABARAP subfamily proteins

Immunoprecipitation of FLAG-ATG8s in HEK293T cells. NEK9 interacted with the GABARAP subfamily, but also with the LC3 subfamily to a lesser extent. Data are representative of three independent experiments.

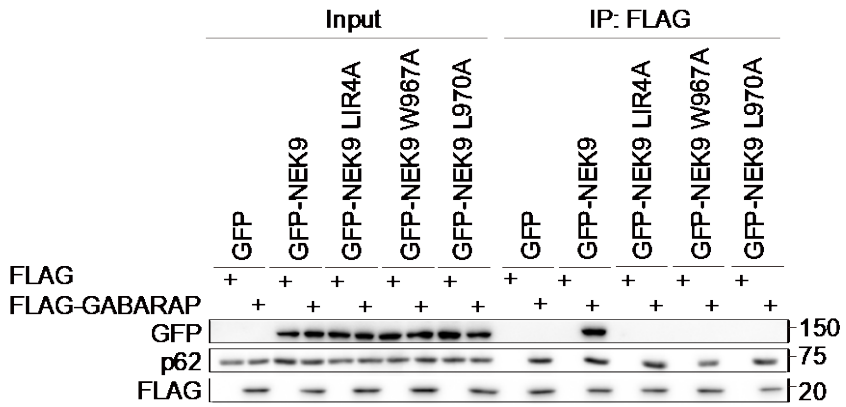

Figure 7. NEK9 interacts with GABARAP in a LIR-dependent manner

Co-immunoprecipitation of FLAG-GABARAP and wild-type or mutant GFP-NEK9 in HEK293T cells. In GFP-NEK9 LIR4A, the LIR residues (WCLL) were substituted by four alanines. Substitution of all four of these residues or even one of the hydrophobic residues (W967 or L970) in the LIR with alanine completely abolished the interaction with GABARAP. These results suggest that the LIR is functional and mediates the NEK9–GABARAP interaction. Data are representative of three independent experiments.

Substitution of all four of these residues or even one of the hydrophobic residues (W967 or L970) in the LIR with alanine completely abolished the interaction with GABARAP (Figure 7). These results suggest that the LIR is functional and mediates the NEK9–GABARAP interaction, consistent with a recent report [47]. Although the overall structure of NEK9 is conserved among all vertebrates, the LIR is present only in land-living vertebrates, including mammals, reptiles, birds, and amphibians, but not in fish. In addition, the LIR is conserved in the coelacanth (*Latimeria chalumnae*), an extant species of ancestral lobe-finned fish from which terrestrial vertebrates evolved [49], suggesting that NEK9's LIR-dependent function is important for terrestrial life (Figure 5).

NEK9 is degraded by selective autophagy.

To investigate the subcellular localization of NEK9, I observed GFP-tagged NEK9 in mouse embryonic fibroblasts (MEFs). Although diffusely distributed in the cytoplasm under nutrient-rich conditions, NEK9 formed punctate structures under autophagy-inducing starvation conditions (Figure 8). NEK9 colocalized with the autophagic membrane marker mRuby3-GABARAP, as well as the isolation membrane markers FIP200 and WIPI2 (Figure 9) [9,10]. In contrast, NEK9 did not form punctate structures in autophagy-deficient *Fip200*-KO cells (Figure 10). A LIR mutant of NEK9 (NEK9 W967A) did not localize to the autophagic membrane, even during starvation (Figure 11).

Thus, NEK9 is associating with the autophagic membrane from an early phase in a LIR-dependent manner. The number of NEK9 puncta increased in the presence of the vacuolar ATPase inhibitor bafilomycin A_1 (Figure 8). Also, NEK9 partially colocalized with lysosome marker LAMP1 under starvation conditions (Figure 9). These data indicate that NEK9 is delivered to lysosomes via autophagy. The level of NEK9 decreased over time during starvation, but this reduction was abolished by bafilomycin A_1 (Figure 12). In contrast, the level of NEK9 did not change during starvation in *Fip200*-KO cells. Furthermore, in *Atg5*$^{-/-}$*;NSE-Atg5* mice, in which autophagy is blocked in all organs except neuronal cells [50], NEK9 accumulated in most organs examined (Figure. 13). These data suggest that NEK9 is degraded by selective autophagy in culture cells and mouse tissues.

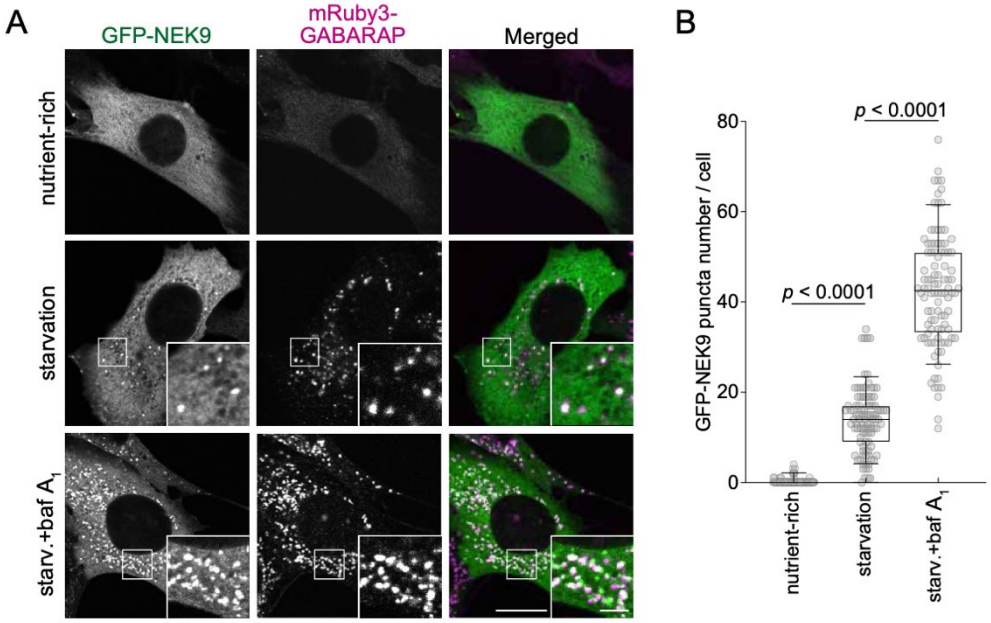

Figure 8. NEK9 is delivered to lysosomes via autophagy

(A) Immunofluorescence microscopy of MEFs expressing GFP-NEK9 and mRuby3-GABARAP under nutrient-rich conditions and amino acid and serum starvation (2 h) conditions with or without 100 nM bafilomycin A_1 (baf A_1). NEK9 associated with autophagic membranes under autophagy-inducing starvation conditions. These data indicate that NEK9 is delivered to lysosomes via autophagy. Data were collected from 100 cells for each condition. Scale bars, 10 μm and 3 μm (insets).

(B) Quantification of the number of NEK9 puncta in **(A)**. Solid bars indicate the medians, boxes the interquartile range (25th to 75th percentile), and whiskers the 10th to 90th percentile. *p*-values correspond to a Tukey's multiple comparisons test.

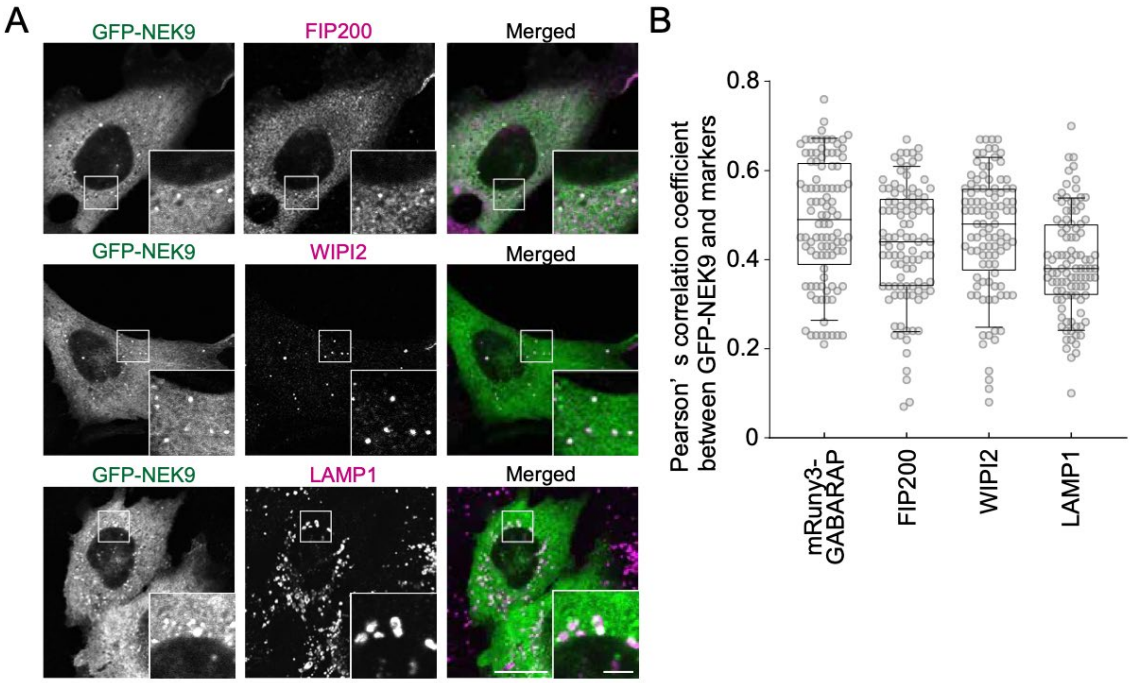

Figure 9. NEK9 associates with the autophagic membrane from an early phase

(A) Immunofluorescence microscopy of wild-type MEFs stably expressing GFP-NEK9 after starvation (2 h). Cells were stained with the indicated antibodies. Scale bars, 10 μm and 3 μm (insets).

(B) Colocalization between GFP-NEK9 and mRuby3-GABARAP (Figure 8), endogenous FIP200, WIPI2, or LAMP1 in **(A)** was determined by calculating Pearson's correlation coefficient between intensities within each cell. Data were collected from 100 cells for each condition. Solid bars indicate the medians, boxes the interquartile range (25th to 75th percentile), and whiskers the 10th to 90th percentile.

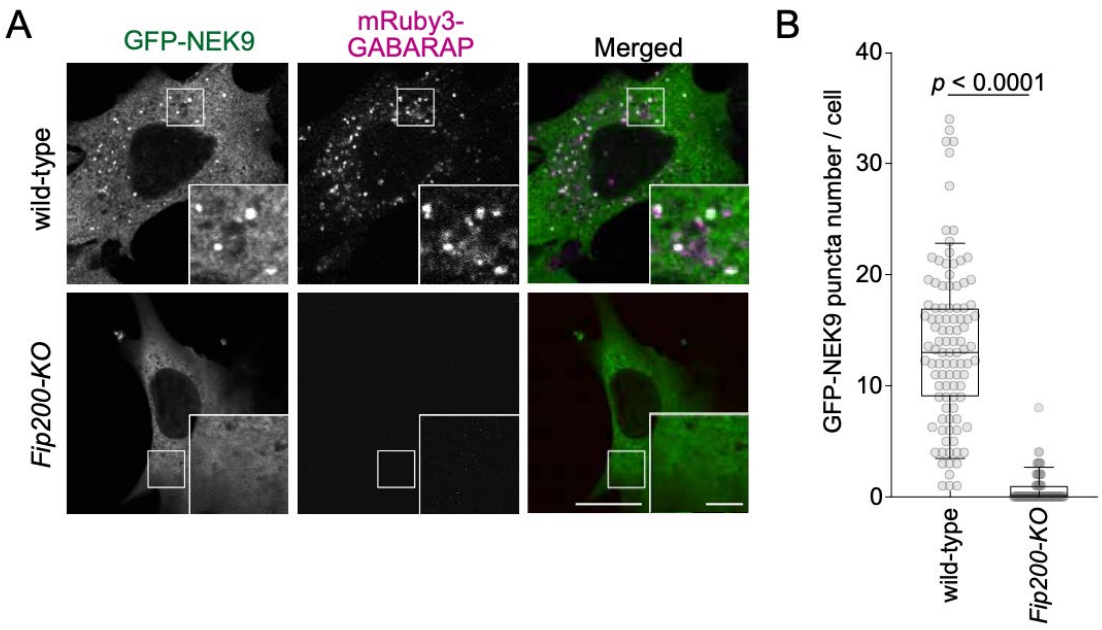

Figure 10. NEK9 did not form punctate structures in autophagy-deficient *Fip200*-KO cells

(A) Immunofluorescence microscopy of wild-type and *Fip200-KO* MEFs expressing GFP-NEK9 after starvation (2 h). Scale bars, 10 μm and 3 μm (insets).

(B,) Quantification of the number of NEK9 puncta in **(A)**. Data were collected from 100 cells for each condition. Solid bars indicate the medians, boxes the interquartile range (25th to 75th percentile), and whiskers the 10th to 90th percentile. *p*-values correspond to two-tailed Mann–Whitney tests.

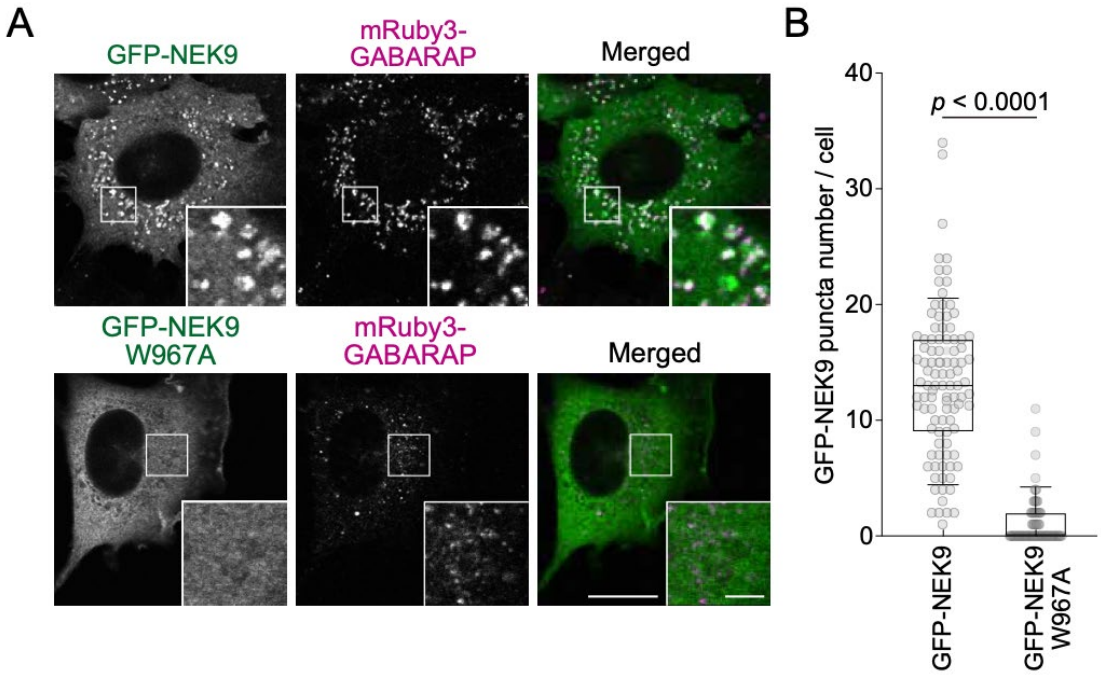

Figure 11. NEK9 localizes to autophagic membranes in a LIR-dependent manner

(A) Immunofluorescence microscopy of wild-type MEFs expressing GFP-NEK9 or GFP-NEK W967A (LIR-mutant) after starvation (2 h). Scale bars, 10 μm and 3 μm (insets). **(B)** Quantification of the number of NEK9 puncta in **(A)**. Data were collected from 100 cells for each condition. Solid bars indicate the medians, boxes the interquartile range (25th to 75th percentile), and whiskers the 10th to 90th percentile. *p*-values correspond to two-tailed Mann–Whitney tests.

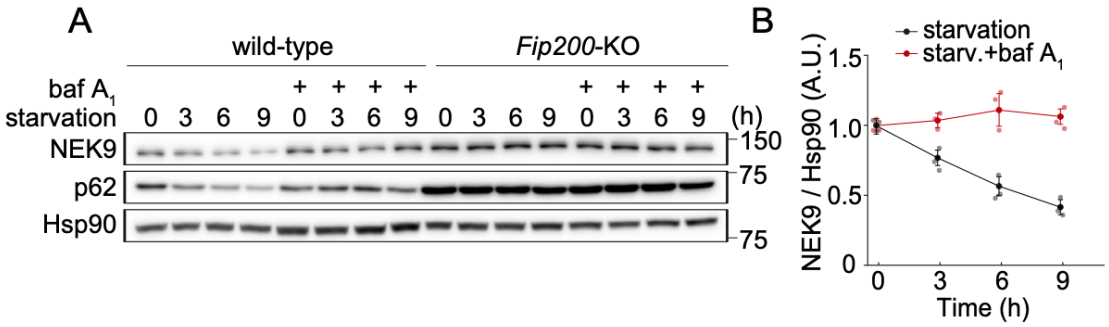

Figure 12. NEK9 is degraded by autophagy in culture cells

(A) Wild-type and *Fip200-KO* MEFs were incubated under starvation conditions with or without 100 nM bafilomycin A_1 for the indicated time. Whole cell lysates were subjected to immunoblotting.

(B) Quantification of the intensity of the NEK9 bands in **(A)**. Data represent the mean ± SEM of three independent experiments.

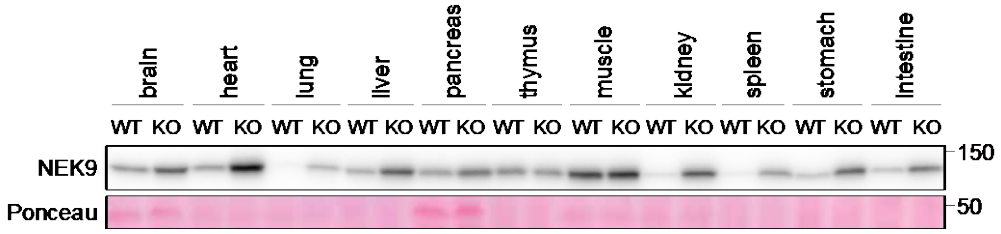

Figure 13. NEK9 is degraded by selective autophagy in mice tissues

Immunoblotting of indicated organs of *Atg*$^{5+/+}$ *(WT) and Atg5*$^{-/-}$*;NSE-Atg5* (KO) mice. Data are representative of three biologically independent replicates.

A recent study proposed that NEK9 suppresses selective autophagy by phosphorylating Thr50 within the LIR-docking site of LC3B; knockdown or knockout of NEK9 enhanced p62 degradation, whereas NEK9-mediated phosphorylation of LC3B suppressed p62 degradation [47]. However, when I depleted NEK9 using three different siNEK9 sequences, I did not observe enhanced p62 degradation (Figure 14). I also generated *Nek9*-KO cells and measured the level of p62 under nutrient-rich and starvation conditions both with and without bafilomycin A_1. Nevertheless, there was no significant difference in p62 level among wild-type cells, *Nek9*-KO cells, and *Nek9*-KO cells re-expressing wild-type NEK9 or a kinase-dead mutant (NEK9 T210A) (Figure 15) [42]. Collectively, I could not observe the inhibitory role of NEK9 in selective autophagy of p62 in my experimental settings; instead, these results indicate that NEK9 is degraded by selective autophagy.

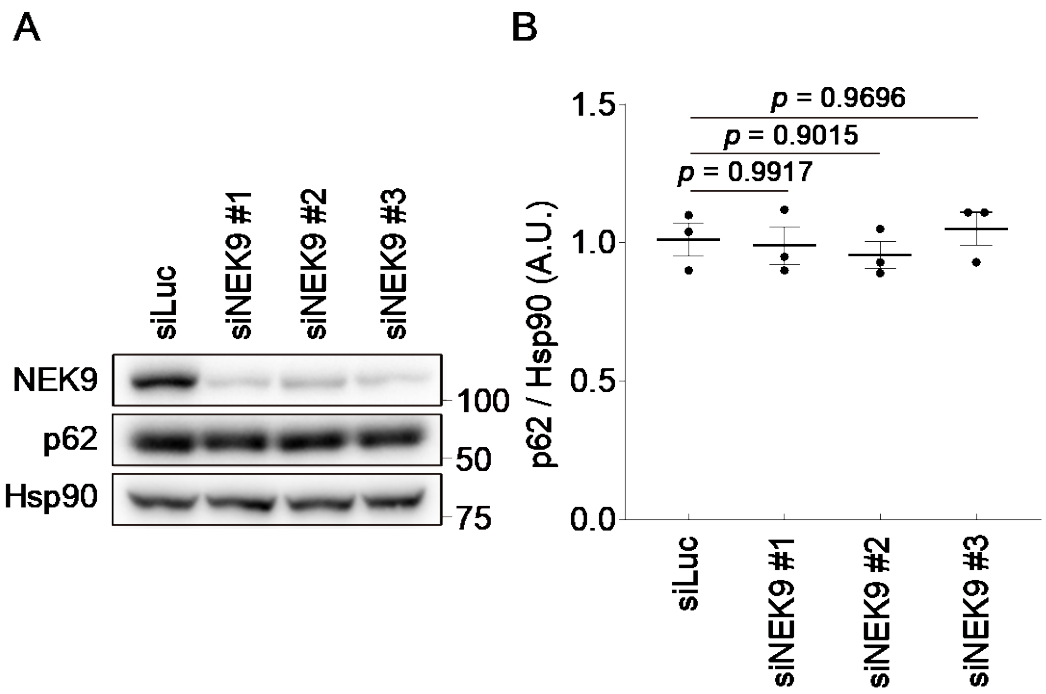

Figure 14. siRNA-mediated depletion of NEK9 does not affect selective autophagy of p62

(A) Immunoblotting of wild-type HeLa cells in which NEK9 was depleted by siRNA-mediated knockdown.

(B) Quantification of the intensity of the NEK9 bands in **(A)**. Data represent the mean ± SEM of three independent experiments. *p*-values correspond to a Tukey's multiple comparisons test.

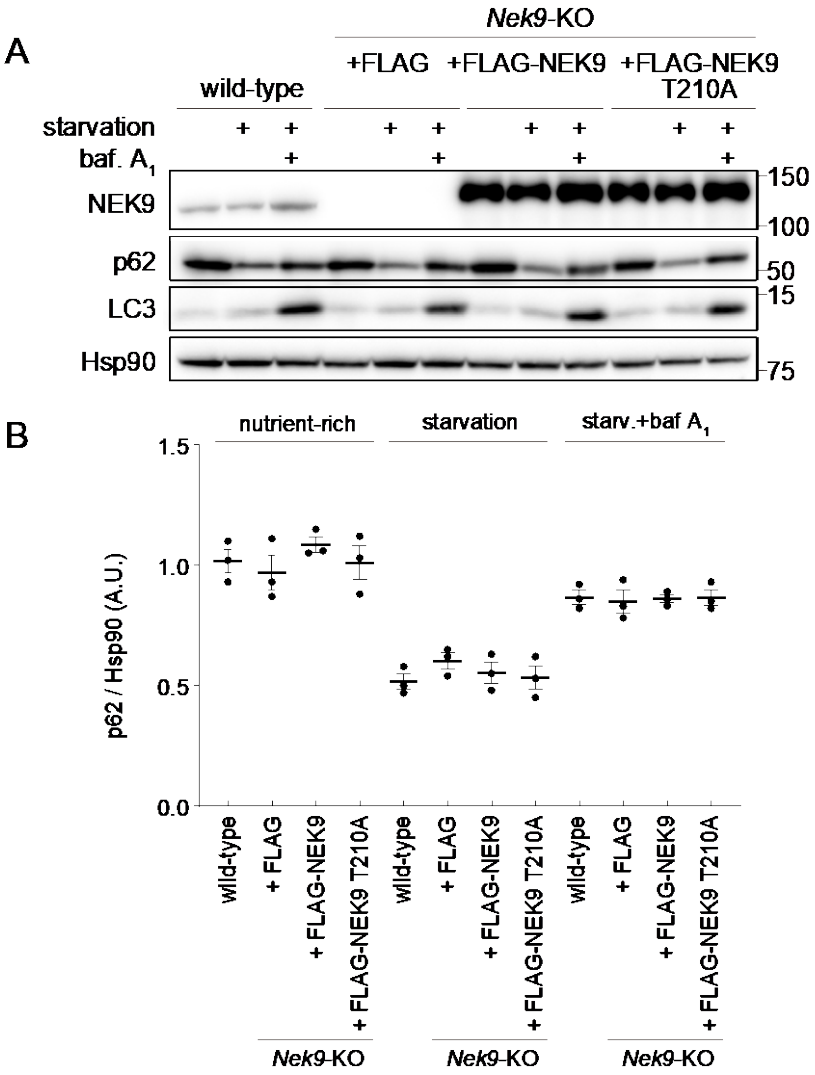

Figure 15. Depletion of NEK9 does not affect selective autophagy of p62

(A) Immunoblotting of wild-type or *Nek9-KO* MEFs stably expressing the indicated constructs under nutrient-rich conditions or after starvation (2 h) with or without 100 nM bafilomycin A1 (baf A1). NEK9 T210A, a kinase-dead mutant NEK9.

(B) Quantification of the intensity of the NEK9 bands. Data represent the mean ± SEM of three independent experiments.

Selective autophagy of NEK9 is required for primary cilia formation.

To investigate NEK9's LIR-dependent function without affecting its kinase activity, I established NEK9 LIR-mutated MEF clones by CRISPR-mediated recombination using a donor plasmid harboring short homology arms (Figure 16) [51]. In these cells, the endogenous W967 residue, which is essential for binding to GABARAPs (Figure 7), was homozygously mutated. NEK9 accumulated in *Nek9*^{W967A} MEFs (Figure 17) and did not localize to autophagic membranes (Figure 18), confirming that NEK9 is degraded by selective autophagy in a LIR-dependent manner.

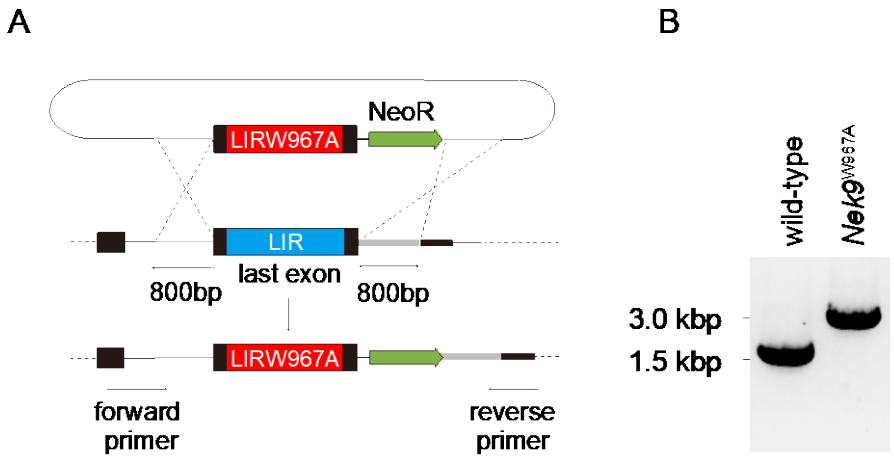

Figure 16. NEK9 LIR-mutated cells were generated by CRISPR-mediated recombination

(A) Generation of homozygous *Nek9*^{W967A} (LIR-mutant) cell lines by CRISPR-mediated recombination using a donor plasmid harboring short homology arms. In these cells, the endogenous W967 residue, which is essential for binding to GABARAPs was homozygously mutated.

(B) Genotyping of *Nek9*^{W967A} MEFs by PCR.

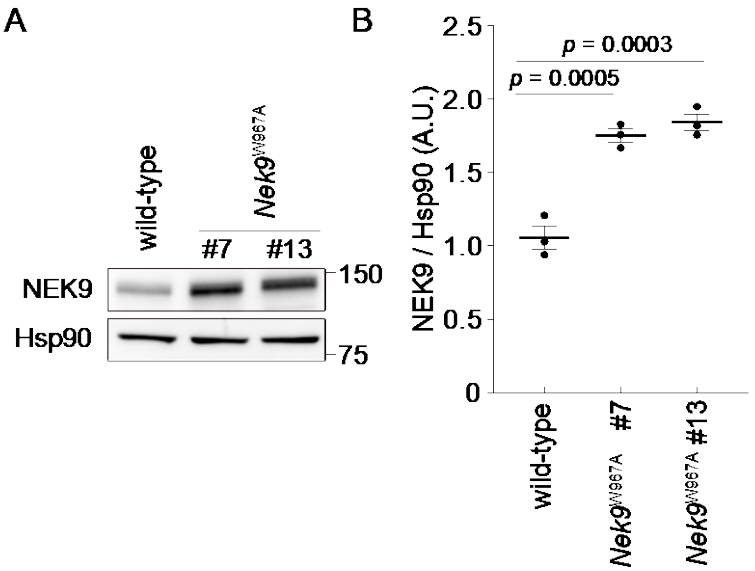

Figure 17. NEK9 accumulates in *Nek9*^{W967A} MEFs

(A) Immunoblotting of wild-type or *Nek9*^{W967A} MEFs (two independent clones, #7 and #13) cultured in nutrient-rich medium.

(B) Quantification of the intensity of the NEK9 bands in **(A)**. Data represent the mean ± SEM of three independent experiments. *p*-values correspond to Tukey's multiple comparisons tests.

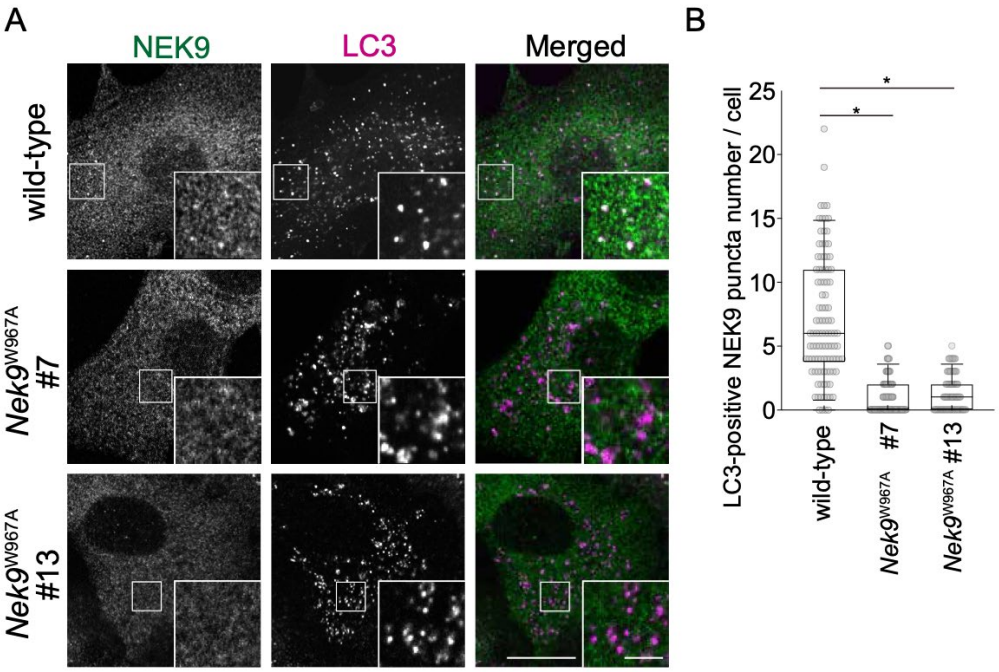

Figure 18. NEK9 does not localize to autophagic membranes in *Nek9*^{W967A} cells

(A) Immunofluorescence microscopy of endogenous NEK9 and LC3 in wild-type or *Nek9*^{W967A} MEFs (two independent clones, #7 and #13) after starvation (2 h). Scale bars, 10 µm and 3 µm (insets).

(B) Quantification of the number of LC3-positive NEK9 puncta in **(A)**. Data were collected from 100 cells for each cell-type. Solid bars indicate the medians, boxes the interquartile range (25th to 75th percentile), and whiskers the 10th to 90th percentile. *p*-values correspond to Tukey's multiple comparisons tests; *$p < 0.0001$.

Based on a previous report suggesting that NEK9 contributes to ciliogenesis through an unknown mechanism [46], I examined primary cilia in *Nek9*^{W967A} MEFs. Centrosome and primary cilia were labeled with anti-pericentrin and ARL13B (a ciliary membrane protein) antibodies, respectively. Primary cilia were formed from basal bodies (mature mother centrioles) under serum starvation conditions [1], but their formation was impaired in *Nek9*^{W967A} MEFs; relative to wild-type MEFs, the frequency of ciliated cells was lower, and cilia length was shorter (Figure 19). To exclude the possibility that this phenotype was cell-type specific, I generated *NEK9*^{W967A} HK-2 cells (human renal proximal tubular cell) and obtained similar results (Figure 20, 21). In my experimental conditions, ciliogenesis was also impaired in autophagy-deficient *Fip200*-KO or *Atg3*-KO MEFs (Figure 22, 23), as previously shown [27-31]. Collectively, these results suggest that LIR-dependent selective autophagy of NEK9 is required for ciliogenesis. To determine whether the kinase activity of NEK9 is required for ciliogenesis, a kinase-dead mutant (NEK9 T210A) was expressed in *Nek9*-KO MEFs [42]. Ciliogenesis was impaired in *Nek9*-KO MEFs, as in *Nek9*^{W967A} MEFs, but it was restored by the expression of the kinase-dead NEK9 T210A but not the LIR-mutant NEK9 W967A (Figure 24). Thus, selective autophagy of NEK9 is required for ciliogenesis, but its kinase activity is not.

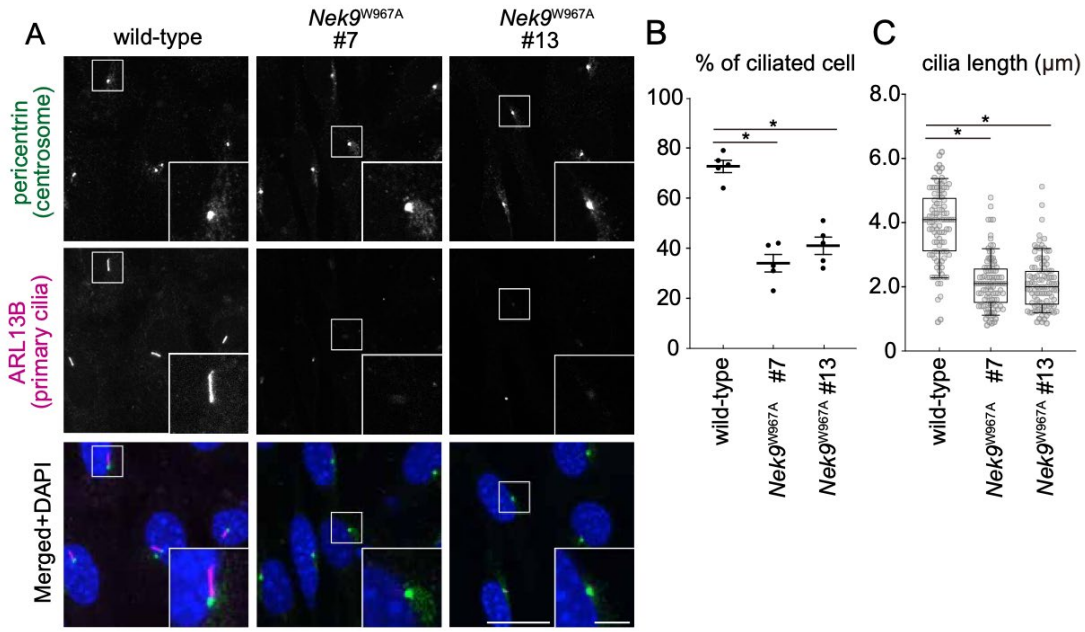

Figure 19. Primary cilia formation is impaired in *Nek9*^{W967A} MEFs

(A) Immunofluorescence microscopy of wild-type or *Nek9*^{W967A} MEFs after serum starvation (24 h). Centrosomes and primary cilia were stained with anti-pericentrin and anti-ARL13B antibodies, respectively. Scale bars, 10 µm and 3 µm (insets).

(B) Frequency of ciliated cells in **(A)**. Data represent the mean ± SEM of five independent experiments (300 cells were counted in each experiment).

(C) Quantification of cilia length in **(A)**. Data were collected from 100 ciliated cells for each cell-type. Solid bars indicate the medians, boxes the interquartile range (25th to 75th percentile), and whiskers the 10th to 90th percentile. *p*-values correspond to Tukey's multiple comparisons tests; *$p < 0.0001$.

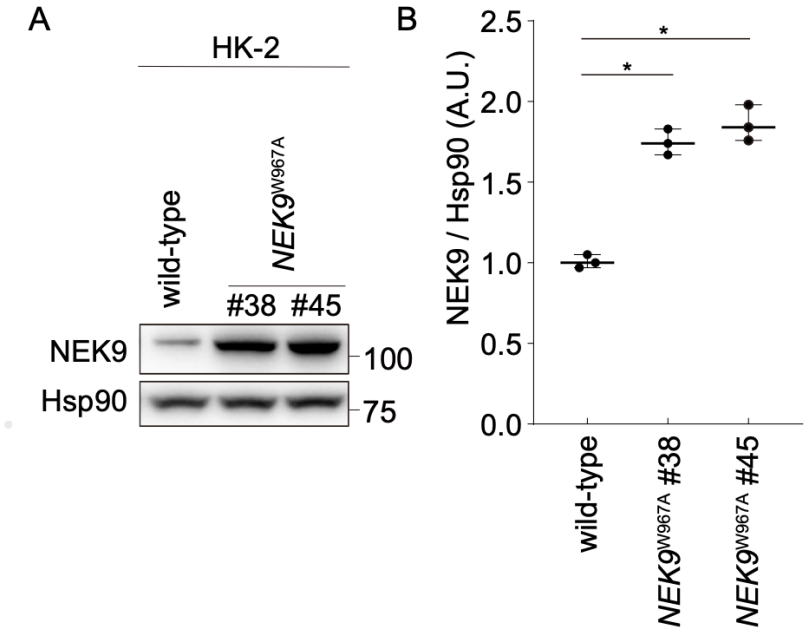

Figure 20. NEK9 accumulates in *NEK9*^{W967A} HK-2 cells

(A) Immunoblotting of wild-type or *NEK9*^{W967A} HK-2 cells (two independent clones, #38 and #45) cultured in nutrient-rich medium.

(B) Quantification of the intensity of the NEK9 bands in **(A)**. Data represent the mean ± SEM of three independent experiments. *p*-values correspond to Tukey's multiple comparisons tests; *$p < 0.0001$.

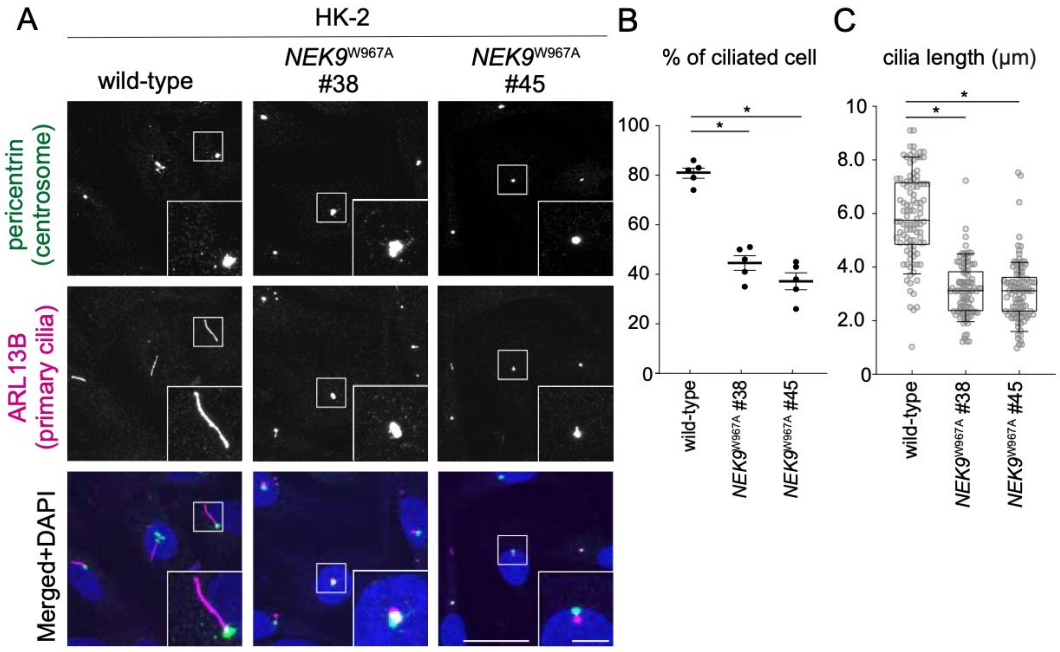

Figure 21. Primary cilia formation is impaired in *NEK9*^{W967A} HK-2 cells

(A) Immunofluorescence microscopy of wild-type or *NEK9*^{W967A} HK-2 cells after serum starvation (24 h). Centrosomes and primary cilia were stained with anti-pericentrin and anti-ARL13B antibodies, respectively. Scale bars, 10 µm and 3 µm (insets).

(B) Frequency of ciliated cells in **(A)**. Data represent the mean ± SEM of five independent experiments (300 cells were counted in each experiment).

(C) Quantification of cilia length in **(A)**. Data were collected from 100 ciliated cells for each cell-type. Solid bars indicate the medians, boxes the interquartile range (25th to 75th percentile), and whiskers the 10th to 90th percentile. *p*-values correspond to Tukey's multiple comparisons tests; *$p < 0.0001$.

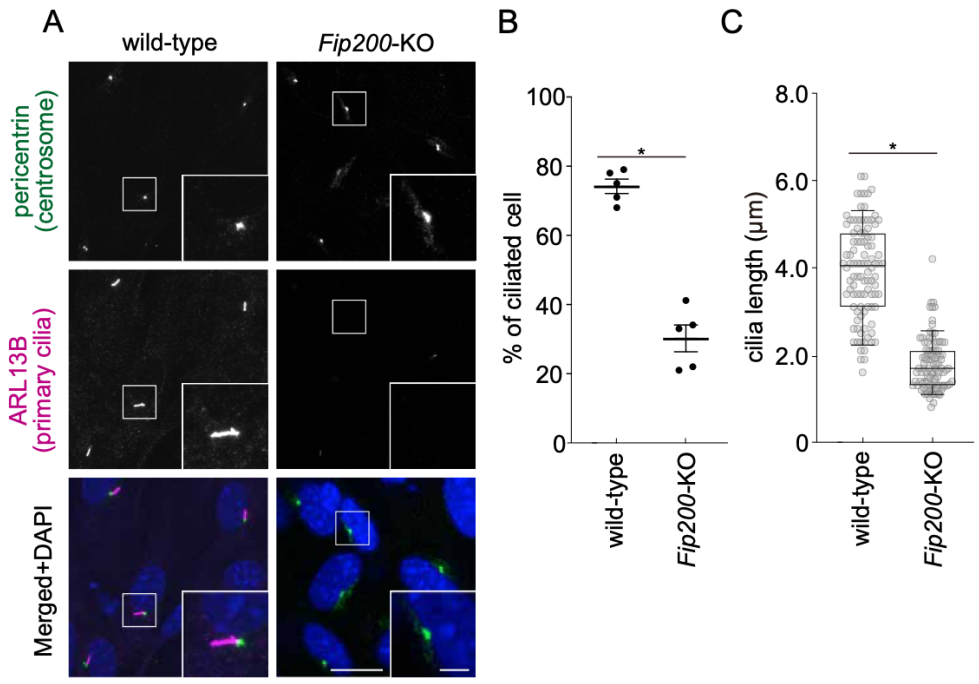

Figure 22. Primary cilia formation is impaired in autophagy-deficient *Fip200-KO* MEFs

(A) Immunofluorescence microscopy of wild-type or *Fip200*-KO MEFs after serum starvation (24 h). Scale bars, 10 µm and 3 µm (insets).

(B) Frequency of ciliated cells in **(A)**. Data represent the mean ± SEM of five independent experiments (300 cells were counted in each experiment).

(C) Quantification of cilia length in **(A)**. Data were collected from 100 ciliated cells for each cell-type. Solid bars indicate the medians, boxes the interquartile range (25th to 75th percentile), and whiskers the 10th to 90th percentile. *p*-values correspond to two-tailed Mann–Whitney tests; *$p < 0.0001$.

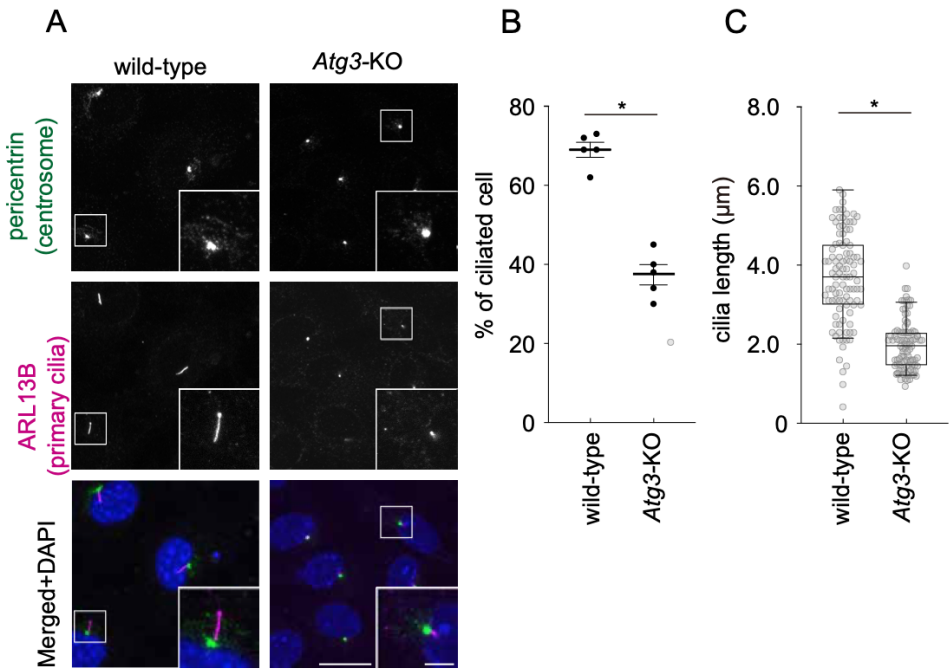

Figure 23. Primary cilia formation is impaired in autophagy-deficient *Atg3-KO* MEFs

(A) Immunofluorescence microscopy of wild-type or *Atg3*-KO MEFs after serum starvation (24 h). Scale bars, 10 µm and 3 µm (insets).

(B) Frequency of ciliated cells in **(A)**. Data represent the mean ± SEM of five independent experiments (300 cells were counted in each experiment).

(C) Quantification of cilia length in **(A)**. Data were collected from 100 ciliated cells for each cell-type. Solid bars indicate the medians, boxes the interquartile range (25th to 75th percentile), and whiskers the 10th to 90th percentile. *p*-values correspond to Tukey's multiple comparisons tests; *$p < 0.0001$.

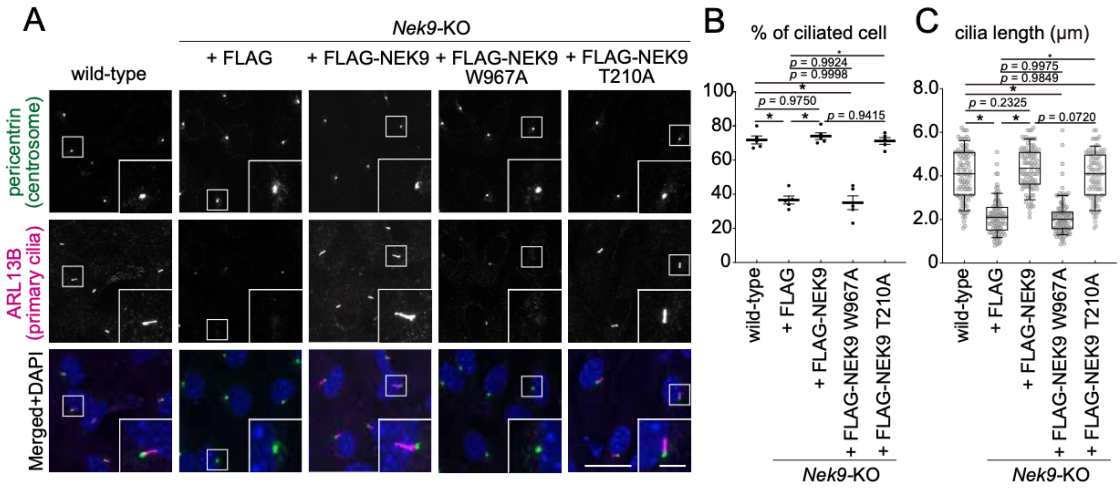

Figure 24. LIR-dependent selective autophagy of NEK9 is required for ciliogenesis, but its kinase activity is not

(A) Immunofluorescence microscopy of wild-type or *Nek9*-KO MEFs stably expressing the indicated constructs after serum starvation (24 h). NEK9 T210A; kinase-dead mutant. Scale bars, 10 μm and 3 μm (insets).

(B) Frequency of ciliated cells in **(A)**. Data represent the mean ± SEM of five independent experiments (300 cells were counted in each experiment).

(C) Quantification of cilia length in **(A)**. Data were collected from 100 ciliated cells for each cell-type. Solid bars indicate the medians, boxes the interquartile range (25th to 75th percentile), and whiskers the 10th to 90th percentile. *p*-values correspond two-tailed Mann–Whitney tests; *$p < 0.0001$.

Selective autophagy of NEK9 is required for primary cilia formation in mouse kidney.

To examine the physiological significance of selective autophagy of NEK9 *in vivo*, a mouse strain harboring the W967A mutation in NEK9 was generated by my collaborator Dr. Tsukamoto (Figure 25A). Although homozygous knockout of *Nek9* was embryonic lethal (MGI: 2387995), homozygous *Nek9*$^{W967A/W967A}$ mice were viable, fertile, and of normal size and weight. In *Nek9*$^{W967A/W967A}$ mice, NEK9 accumulated in most organs tested, particularly in the kidney (Figure 25B), confirming that NEK9 is degraded by selective autophagy *in vivo*.

The kidney is one of the most frequently affected organs in ciliopathies with primary cilia dysfunction [2,8]. I examined primary cilia of proximal tubular cells in the cortical region of the kidneys and found that primary cilia formation was impaired in *Nek9*$^{W967A/W967A}$ mice (Figure 26); relative to wild-type littermates, the frequency of ciliated cells was lower in *Nek9*$^{W967A/W967A}$ mice, and cilia length was also shorter. As previously observed in proximal tubule-specific *Atg7*-KO mice [30], I also observed impaired ciliogenesis in renal tubular cells of *Atg5*$^{-/-}$*;NSE-Atg5* mice (Figure 27). These results suggest that selective autophagy of NEK9 is required for primary cilia formation *in vivo*.

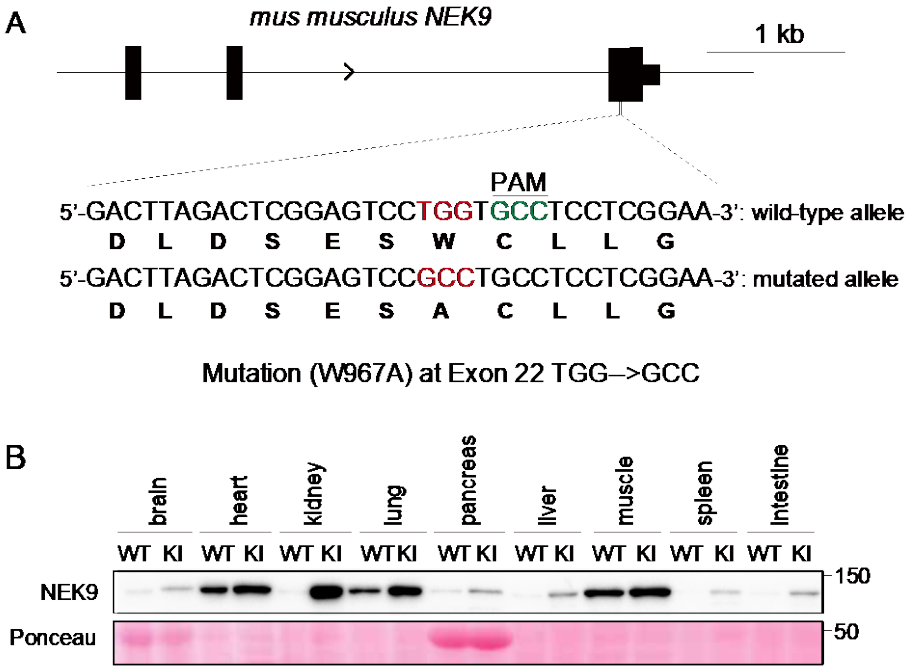

Figure 25. A mouse strain harboring the W967A mutation in NEK9 is generated

(A) Strategy of the CRISPR-mediated knockin of the W967A mutation at the mouse *Nek9* genomic locus. The protospacer-adjacent motif (PAM) sequence is shown in green. **(B)** Immunoblotting of the indicated organs of wild-type (WT) and *Nek9*$^{W967A/W967A}$ mice (KI). Data are representative of three biologically independent replicates.

Previous reports suggest that primary cilia negatively regulate cell size through downregulating mTOR activity, and impaired ciliogenesis results in secondary cellular hypertrophy [52]. In ciliopathy models like *Kif3a*-deficient mice, enlarged cells were observed in renal tubules [53]. Consistently, *Nek9*$^{W967A/W967A}$ mice showed hypertrophy of proximal renal tubular cells (Figure 26D). Similar result was obtained when I evaluated all renal tubular cells in the cortex area by Hematoxylin and eosin staining (Figure28). Furthermore, previous reports have shown cellular hypertrophy in renal tubular cells of autophagy-deficient mice [50,54]. Given that the magnitude of cellular hypertrophy was similar between *Nek9*$^{W967A/W967A}$ and *Atg5*$^{-/-}$*;NSE-Atg5* kidneys (Figure 27D and Figure 29), these results imply that the cellular hypertrophy previously observed in autophagy-deficient kidneys could be largely due to disturbed primary cilia formation resulting from a defect in selective autophagy of NEK9.

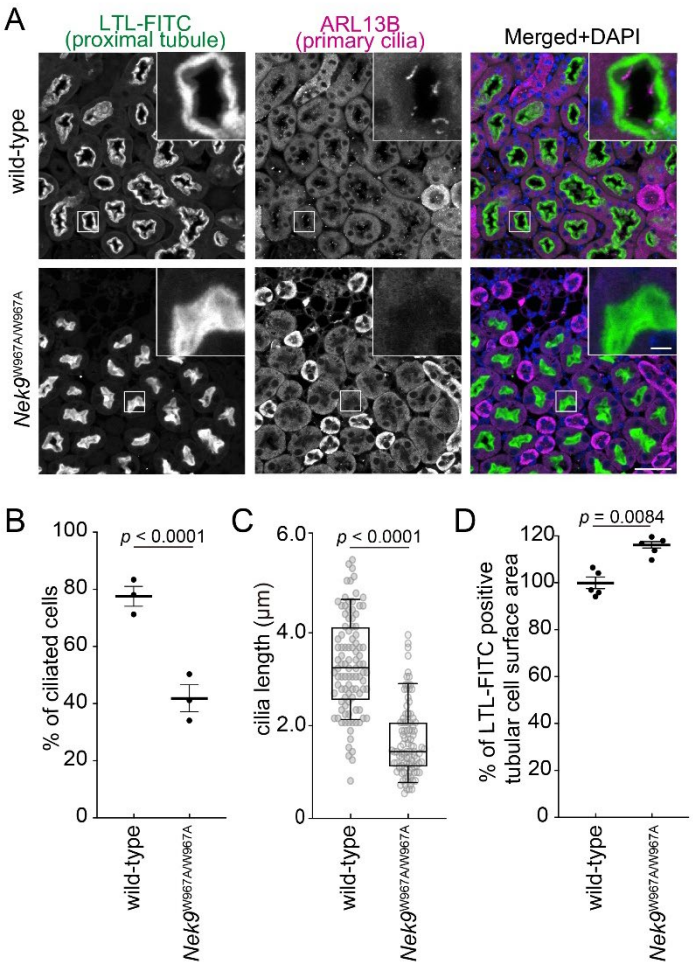

Figure 26. Selective autophagy of NEK9 is required for primary cilia formation in mouse kidney

(A) Immunohistochemistry of the cortical region of kidneys from wild-type and *Nek9*$^{W967A/W967A}$ mice using LTL-FITC (the lumen of proximal-tubular cells) and anti-ARL13B antibody (primary cilia). Scale bars, 40 µm and 5 µm (insets).

(B) Frequency of ciliated cells in LTL-FITC positive cells in **(A)**. Data represent the mean ± SEM of three mice (300 cells were counted in each experiment).

(C) Quantification of cilia length in LTL-FITC positive cells in **(A)**. Data were collected from 100 ciliated cells for each genotype. *p*-values correspond to two-tailed Mann–Whitney tests.

(D) Measurement of the surface area of LTL-FITC positive tubular cells in **(A)**. Data represent the mean ± SEM of five mice (300 cells were counted in each experiment). *p*-values correspond to two-tailed Mann–Whitney tests.

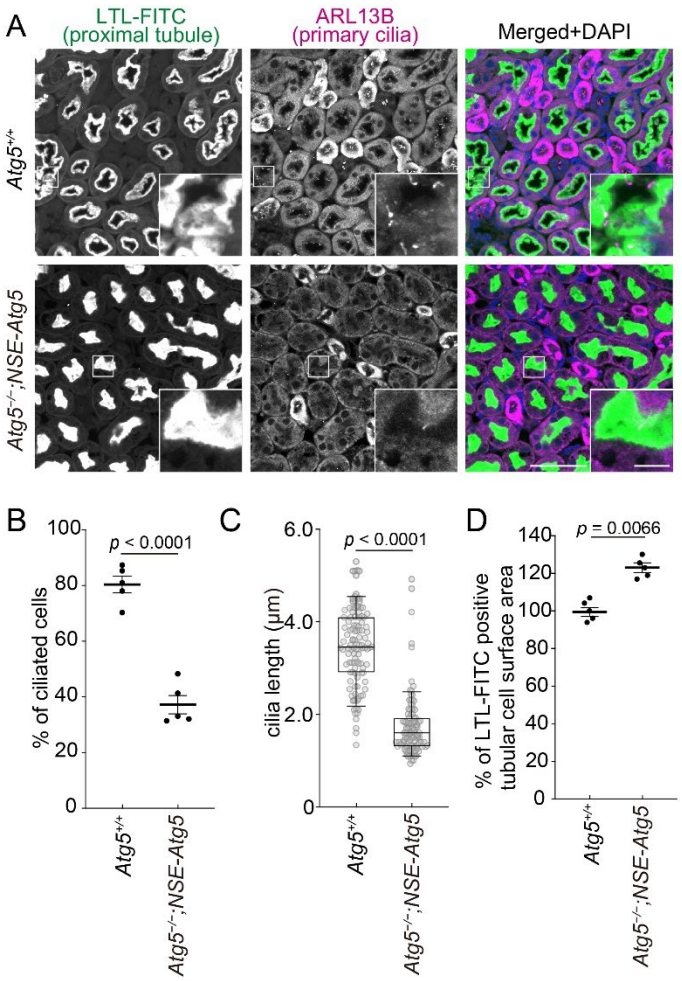

Figure 27. Primary cilia formation is impaired in the kidney of *Atg5*$^{-/-}$*;NSE-Atg5* mice

(A) Immunohistochemistry of the cortical region of kidneys from *Atg5*$^{+/+}$ and *Atg5*$^{-/-}$*;NSE-Atg5* mice using LTL-FITC (the lumen of proximal-tubular cells) and anti-ARL13B antibody (primary cilia). Scale bars, 40 μm and 5 μm (insets).

(B) Frequency of ciliated cells in LTL-FITC positive cells in **(A)**. Data represent the mean ± SEM of three mice (300 cells were counted in each experiment).

(C) Quantification of cilia length in LTL-FITC positive cells in **(A)**. Data were collected from 100 ciliated cells for each genotype. *p*-values correspond to two-tailed Mann–Whitney tests.

(D) Measurement of the surface area of LTL-FITC positive tubular cells in **(A)**. Data represent the mean ± SEM of five mice (300 cells were counted in each experiment). *p*-values correspond to two-tailed Mann–Whitney tests.

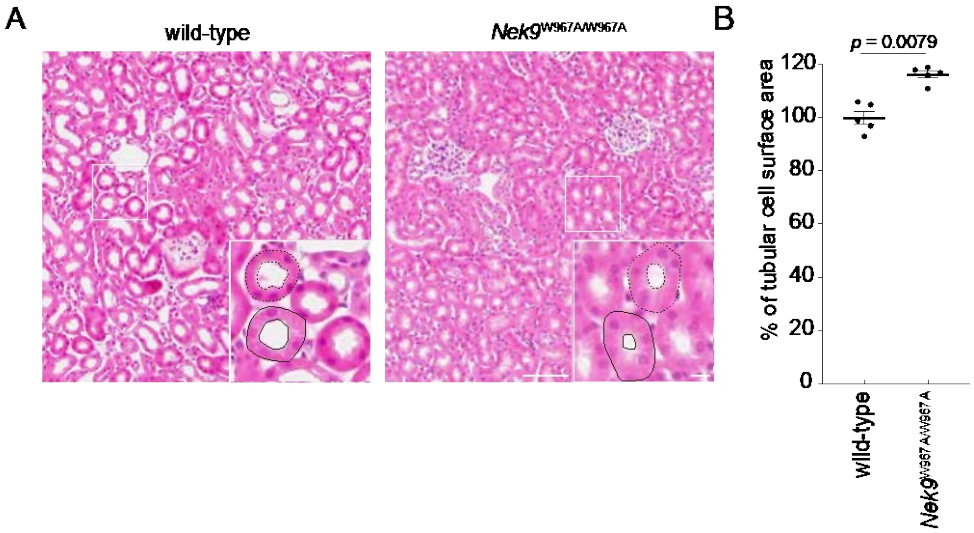

Figure 28. *Nek9*$^{W967A/W967A}$ mice showed hypertrophy of renal tubular cells

(A) Hematoxylin and eosin staining of the cortical region of kidneys from wild-type and *Nek9*$^{W967A/W967A}$ mice. Scale bars, 100 µm and 10 µm (insets).

(B) Measurement of the surface area of tubular cells in **(A)**. Examples of measured areas are shown with broken lines in **(A)**. Data represent the mean ± SEM of five mice (300 cells were counted in each experiment). *p*-values correspond to two-tailed Mann–Whitney tests.

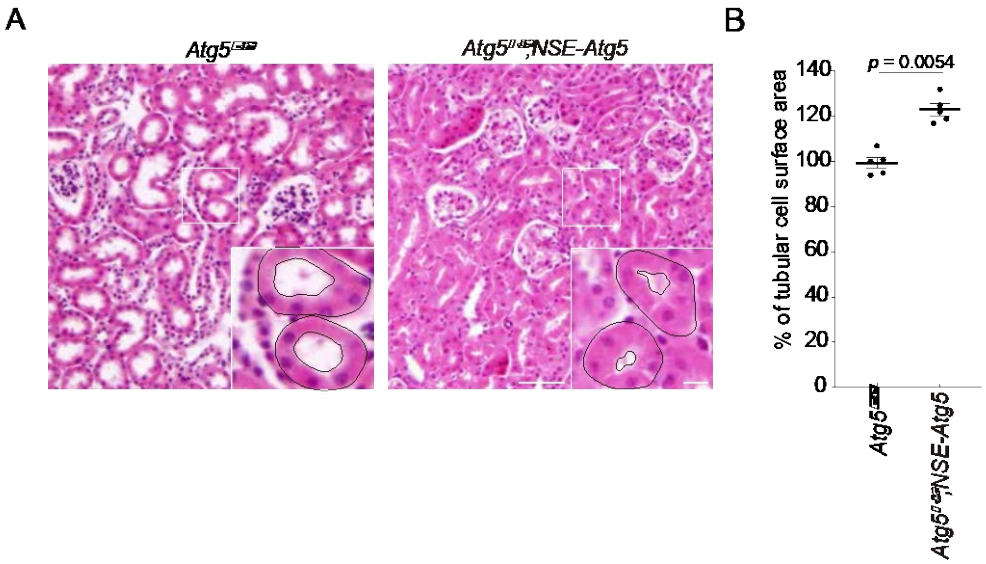

Figure 29. *Atg5*$^{-/-}$*;NSE-Atg5* mice showed hypertrophy of renal tubular cells

(A) Immunohistochemistry of the cortical region of kidneys from *Atg5*$^{+/+}$ and *Atg5*$^{-/-}$*;NSE-Atg5* mice using LTL-FITC (the lumen of proximal-tubular cells) and anti-ARL13B antibody (primary cilia). Scale bars, 40 μm and 5 μm (insets).

(B) Frequency of ciliated cells in LTL-FITC positive cells in **(A)**. Data represent the mean ± SEM of three mice (300 cells were counted in each experiment).

(C) Quantification of cilia length in LTL-FITC positive cells in **(A)**. Data were collected from 100 ciliated cells for each genotype. Solid bars indicate the medians, boxes the interquartile range (25th to 75th percentile), and whiskers the 10th to 90th percentile. *p*-values correspond to two-tailed Mann–Whitney tests.

NEK9 is a selective autophagy adaptor for MYH9

There are two possible explanations for ciliogenesis impairment in *Nek9*$^{W967A/W967A}$ mice: (1) accumulated NEK9 may inhibit ciliogenesis, and (2) NEK9 may act as an autophagy adaptor for a ciliogenesis inhibitory protein. The former is unlikely because ciliogenesis was intact in NEK9-overexpressing cells (Figure 30) and in heterozygous *Nek9*$^{WT/W967A}$ mice (Figure 31), despite the accumulation of NEK9. In contrast, ciliogenesis was affected in *Nek9*-KO MEFs (Figure 24). Thus, I hypothesized that NEK9 functions as a selective autophagy adaptor that binds to and degrades a suppressor of ciliogenesis.

NEK9 did not localize to the cilium or basal body under serum starvation conditions (Figure 32), suggesting that cilia components are not cargos of NEK9. In collaboration with Drs. Ode and Ueda, immunoprecipitation and mass spectrometry analysis using FLAG-NEK9 was performed to identify NEK9-interacting proteins. Among the 43 potential interacting proteins (Figure 33, Table2), those with more than five-fold enrichment in the FLAG-NEK9 immunoprecipitates relative to the FLAG-only immunoprecipitates were individually tested for actual interaction with NEK9. I found that NEK9 specifically interacted with MYH9, an isoform of non-muscle myosin II (Figure 34) [55].

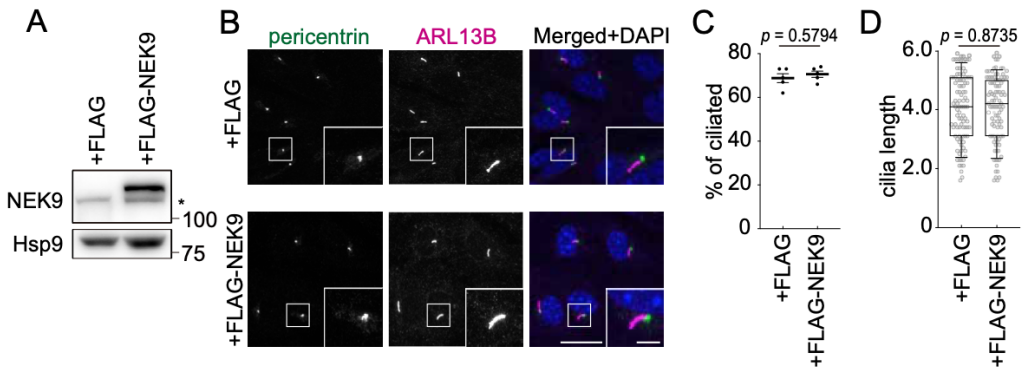

Figure 30. Primary cilia formation is intact in NEK9-overexpressing cells

(A) Immunoblotting of wild-type MEFs stably expressing FLAG or FLAG-NEK9. The asterisk indicates endogenous NEK9.

(B) Immunofluorescence microscopy of wild-type MEFs stably expressing FLAG or FLAG-NEK9 after serum starvation (24 h). Scale bars, 10 μm and 3 μm (insets).

(C) Frequency of ciliated cells in **(B)**. Data represent the mean ± SEM of five independent experiments (300 cells were counted in each experiment).

(D) Quantification of cilia length in **(B)**. Data were collected from 100 ciliated cells for each cell-type. Solid bars indicate the medians, boxes the interquartile range (25th to 75th percentile), and whiskers the 10th to 90th percentile. *p*-values correspond to two-tailed Mann–Whitney tests.

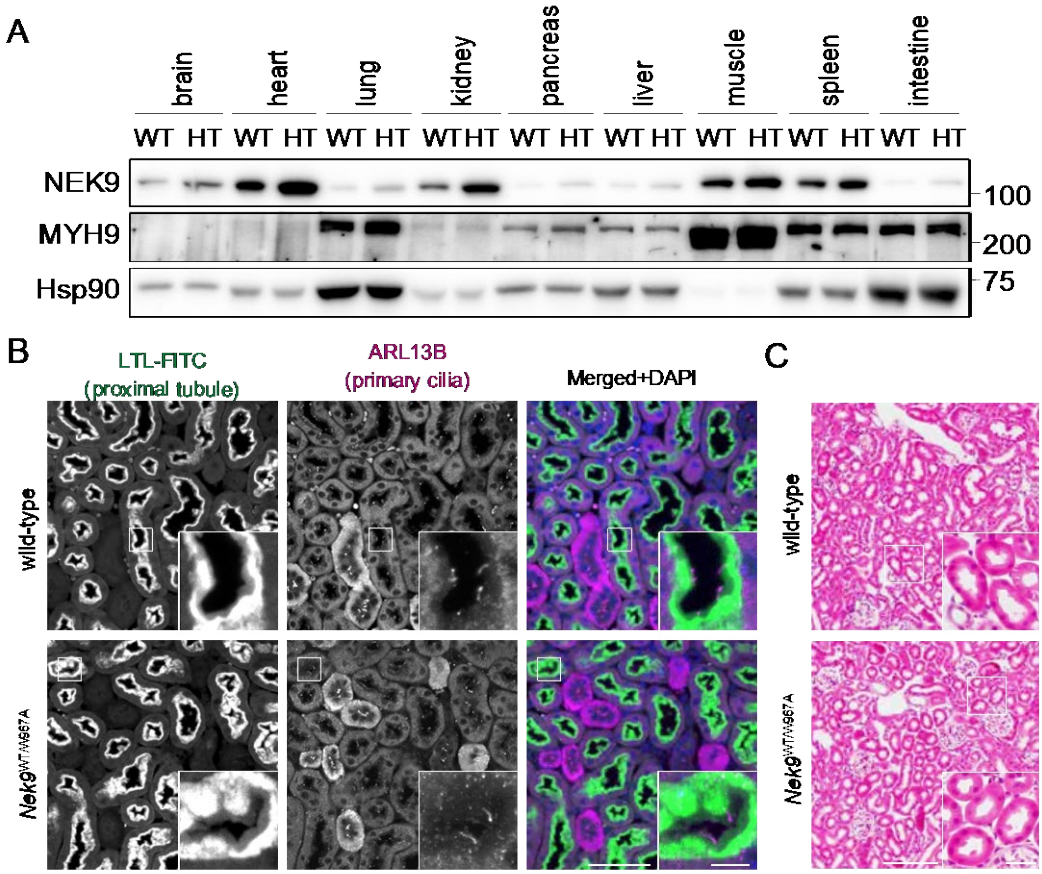

Figure 31. Primary cilia formation is intact in the kidneys of *Nek9*$^{WT/W967A}$ mice

(A) Immunoblotting of the indicated organs of wild-type (WT) and *Nek9*$^{WT/W967A}$ mice (HT). Data are representative of three biologically independent replicates.

(B) Immunohistochemistry of the cortical region of kidneys from wild-type and heterozygous *Nek9*$^{WT/W967A}$ mice. Scale bars, 40 μm and 5 μm (insets).

(C) Hematoxylin and eosin staining of the cortical region of kidneys from wild-type and *Nek9*$^{WT/W967A}$ mice. Scale bars, 100 μm and 10 μm (insets).

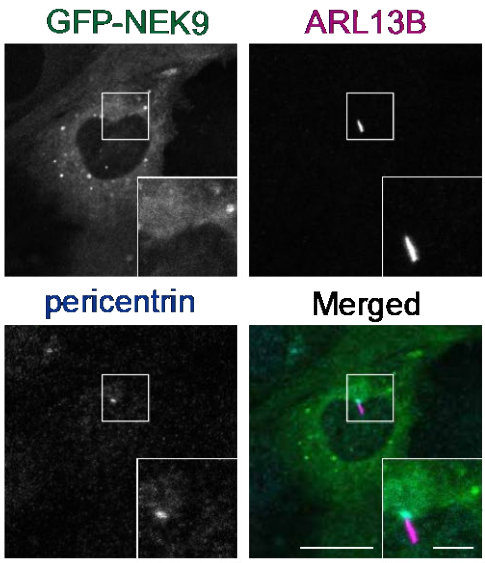

Figure 32. NEK9 does not localize to the centrosome or primary cilium

Immunofluorescence microscopy of wild-type MEFs stably expressing GFP-NEK9 after serum starvation (24 h), showing that NEK9 does not localize to the centrosome (pericentrin) or cilia (ARL13B). Scale bars, 10 μm and 3 μm (insets).

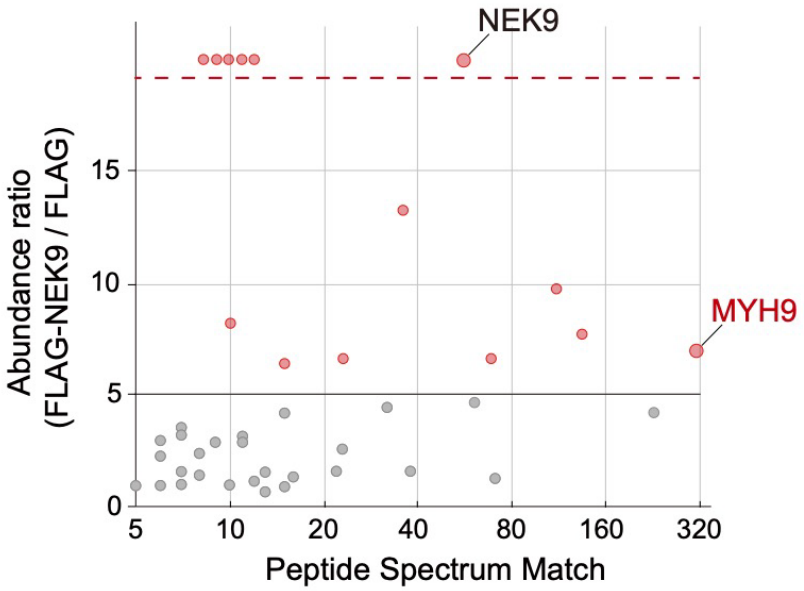

Figure 33. Immunoprecipitation and mass spectrometry analysis using FLAG-NEK9 revealed potential NEK9-interacting proteins

Results of mass spectrometry analysis of FLAG-NEK9 or FLAG immunoprecipitates. The *x*- and *y*-axes represent Peptide Spectrum Match (PSM) and abundance ratio (FLAG-NEK9 / FLAG), respectively. Proteins above the dotted line were detected only in FLAG-NEK9 immunoprecipitates.

Table 2. The results of immunoprecipitation and mass spectrometry analysis using FLAG-NEK9

Immunoprecipitation and mass spectrometry (MS) using FLAG or FLAG-NEK9 were performed. All 43 detected proteins are listed. Peptide Spectrum Match (PSM) and the abundance ratio (FLAG-NEK9 / FLAG) are shown.

Description	# PSMs	Abundance Ratio (FLAG-NEK9 / FLAG)
NEK9	56	20
Plectin	12	20
Filamin-A	11	20
myosin-Ic	10	20
MYL9	9	20
Filamin-B	8	20
Vimentin	36	13.285
Myosin-10	111	9.766
Lima1	10	8.252
Actin, muscle	135	7.816
MYH9	314	6.964
MYL6	23	6.425
Tpm1	69	6.377
MYL12B	15	6.259
Tpm2	57	4.87
Actin, cytoplasmic	223	4.639
Tpm3	32	4.433
Capzb	15	4.184
Capza1	7	3.533
Arpc4	7	3.199
Arpc2	11	3.145
Arpc3	6	2.95
Tpm4	11	2.878
Capza2	9	2.876
Gsn	23	2.567
Actr3	8	2.374

Arpc5	6	2.255
Tmod3	22	1.582
Txndc12	38	1.58
Coro1c	7	1.565
Hspa5	13	1.542
Actn1	8	1.4
Hspa8	16	1.326
Mthfd1	71	1.255
Ppm1b	12	1.135
Stk38	7	0.984
Calm2	10	0.967
Eif4b	6	0.943
Kctd5	5	0.934
Cfl1	15	0.889
Actn4	13	0.658
Vcp	5	0.548

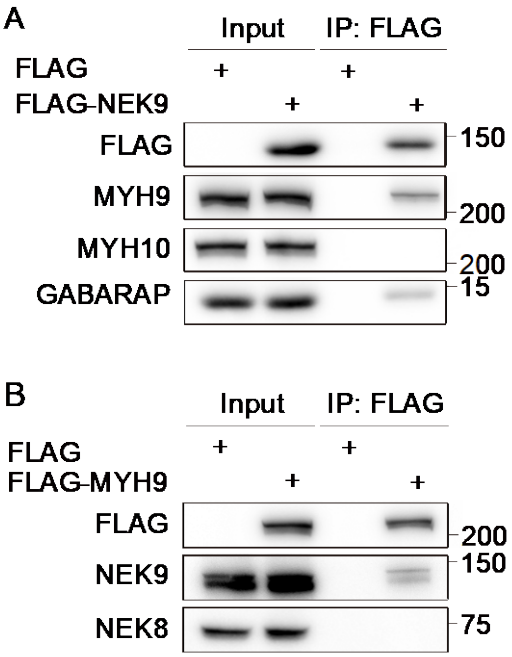

Figure 34. MYH9 interacts with NEK9

(A) Immunoprecipitation using MEFs stably expressing FLAG or FLAG-NEK9 after serum starvation (4 h). Data are representative of three independent experiments.

(B) Immunoprecipitation using MEFs stably expressing FLAG or FLAG-MYH9. after serum starvation (4 h). Data are representative of three independent experiments.

Recent evidence has shown that primary cilia formation is both actin- and microtubule-dependent [56-58]. When ciliogenesis is initiated during cellular quiescence, dynamic remodeling of actin and microtubule cytoskeletons occurs. This enables subsequent migration of the centrosome toward the apical cell surface, where the mother centriole matures into the basal body and the cilium elongates [56,59]. If branched F-actin is stabilized, it impairs the recruitment of ciliogenesis effectors such as RAB11-positive recycling endosomes to the pericentrosomal preciliary compartment, thereby inhibiting the supply of new membranes and proteins to support cilium growth [56, 60-62]. Hence, dynamic actin-network remodeling is required for efficient ciliogenesis.

Non-muscle myosin II is an actin-motor protein that has actin cross-linking and contractile abilities. There are three mammalian isoforms (MYH9, myosin IIA; MYH10, myosin IIB; MYH11, myosin IIC), which have both overlapping and unique properties [63]. Myosin II has a central role in cell adhesion, cell migration, and tissue architecture [55,64,65] and is also involved in primary cilia formation [56,59,66,67]. MYH9 suppresses actin dynamics by stabilizing the actin filament network and is hypothesized to be a negative regulator of ciliogenesis [66]. In contrast, MYH10 promotes ciliogenesis by antagonizing MYH9 [66,67].

GFP-tagged MYH9 formed punctate structures in wild-type cells under serum starvation conditions and colocalized with LC3 and NEK9, indicating that MYH9 associates with autophagic membranes; In contrast, MYH9 did not form punctate structures in *Nek9*^{W967A} cells in which NEK9 is not anchored to autophagic membranes (Figure 35). Thus, NEK9 recruits MYH9 to autophagic membranes. MYH9 accumulated in *Nek9*^{W967A} cells (Figure 36), *Fip200*-KO cells (Figure 37), and organs of *Nek9*$^{W967A/W967A}$ mice (Figure 38) and *Atg5*$^{-/-}$*;NSE-Atg5* mice (except the brain, heart, and muscles, in which MYH9 is not expressed [68]) (Figure 39). Although MYH9 and MYH10 are supposed to interact and form hetero-oligomers [63,66], MYH10 did not interact with NEK9 (Figure 34) or accumulate in *Nek9*$^{W967A/W967A}$ or *Atg5*$^{-/-}$*;NSE-Atg5* mice (Figure 38, 39). These data suggest that MYH9 is a substrate of selective autophagy that is specifically mediated by NEK9 in a LIR-dependent manner.

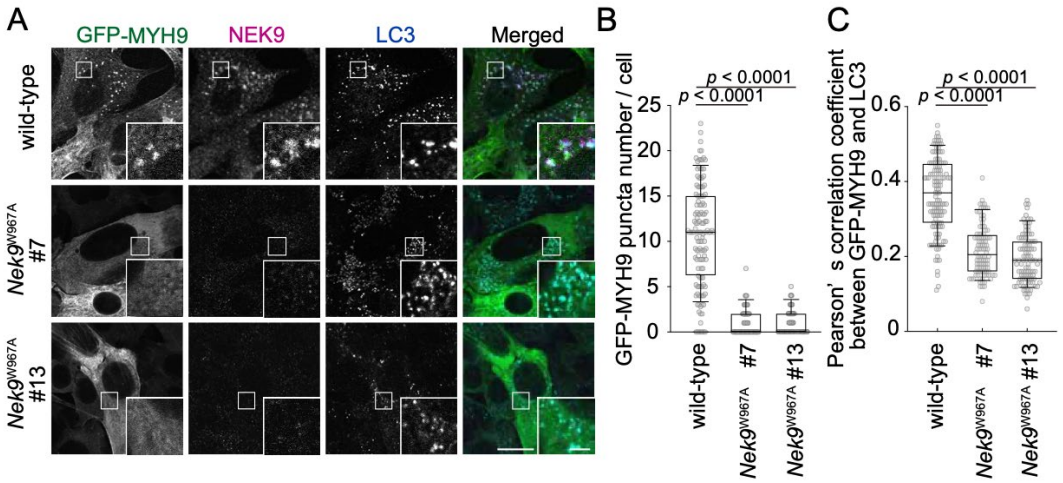

Figure 35. NEK9 recruits MYH9 to autophagic membranes

(A) Immunofluorescence microscopy of wild-type and *Nek9*^{W967A} MEFs stably expressing GFP-MYH9 after serum-starvation (4 h). Cells were stained with anti-NEK9 and anti-LC3 antibodies. Scale bars, 10 μm and 3 μm (insets).

(B) Quantification of the number of GFP-MYH9 puncta in **(A)**.

(C) Colocalization between GFP-MYH9 and endogenous LC3 in **(A)** was determined by calculating Pearson's correlation coefficient between intensities within each cell. Data were collected from 100 cells for each cell-type. Solid bars indicate the medians, boxes the interquartile range (25th to 75th percentile), and whiskers the 10th to 90th percentile. *p*-values correspond to Tukey's multiple comparisons tests.

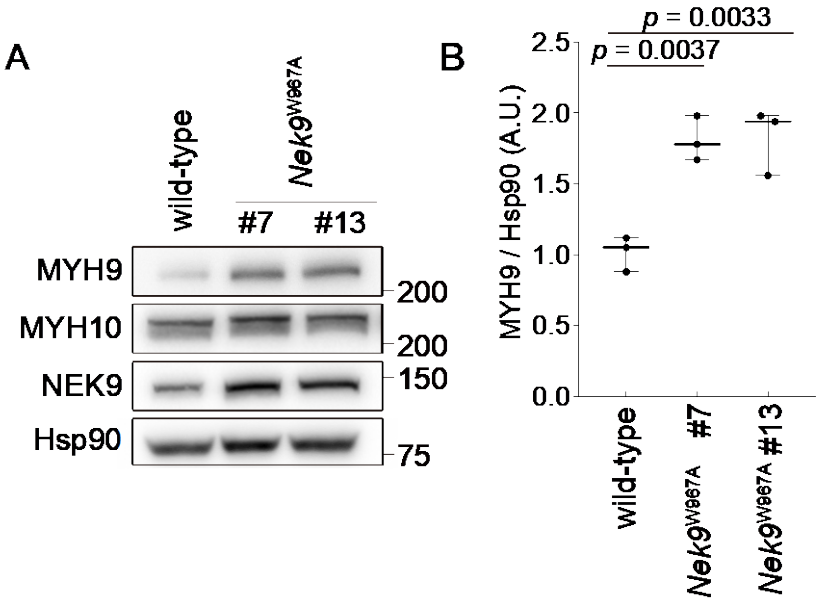

Figure 36. MYH9 accumulates in *Nek9*^{W967A} MEFs

(A) Immunoblotting of wild-type and *Nek9*^{W967A} MEFs.

(B) Quantification of the intensity of the MYH9 bands in **(A)**. Data represent the mean ± SEM of three independent experiments. *p*-values correspond to Tukey's multiple comparisons tests.

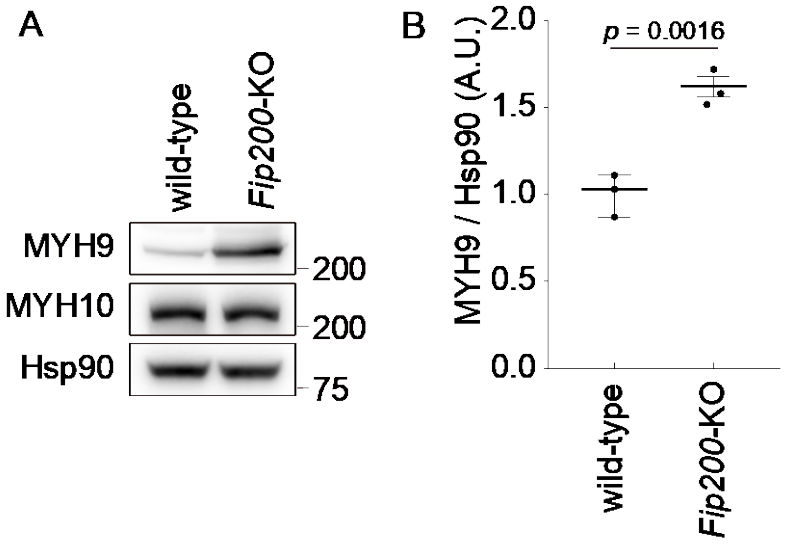

Figure 37. MYH9 accumulates in *Fip200-KO* MEFs

(A) Immunoblotting of wild-type or *Fip200*-KO MEFs.

(B) Quantification of the intensity of the MYH9 bands in **(A)**. Data represent the mean ± SEM of three independent experiments. *p*-values correspond to two-tailed Mann–Whitney tests.

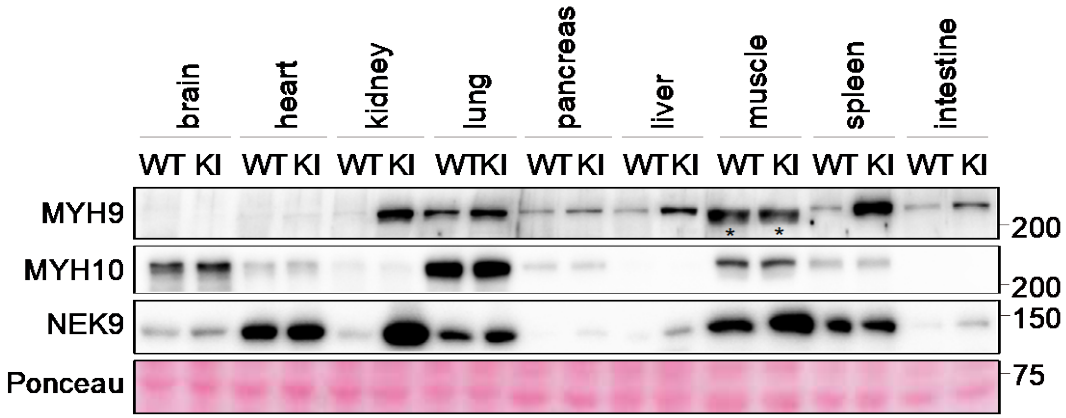

Figure 38. MYH9 accumulates in most organs of *Nek9*$^{W967A/W967A}$

Immunoblotting of the indicated organs of wild-type (WT) and *Nek9*$^{W967A/W967A}$ mice (KI). Asterisks (*) indicate non-specific bands in skeletal muscles. Data are representative of three biologically independent replicates.

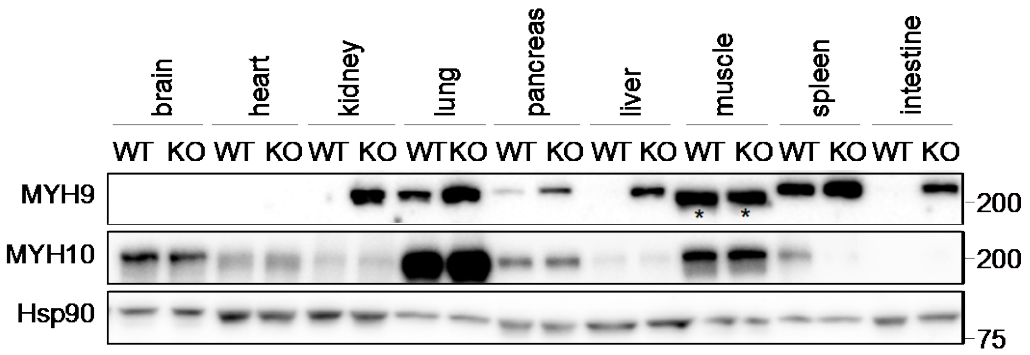

Figure 39. MYH9 accumulates in most organs of *Atg5*$^{-/-}$*;NSE-Atg5* mice

Immunoblotting of the indicated organs of wild-type (WT) and *Atg5*$^{-/-}$*;NSE-Atg5* mice (KO). Asterisks (*) indicate non-specific bands in skeletal muscles. Data are representative of three biologically independent replicates.

NEK9-mediated selective autophagy of MYH9 is required for primary cilia formation

When MYH9 was overexpressed in wild-type MEFs, primary cilia formation was impaired (Figure 40), confirming a previous report that MYH9 is a suppressor of ciliogenesis [66]. Next, I generated truncated NEK9 constructs to find an MYH9-binding region (Figure 41A). Mutants lacking the C-terminal region downstream of the LIR (residues 973–979) did not bind to MYH9 (Figure 41B), suggesting that the region comprising residues 973–979 is important for MYH9 binding. Like the LIR in NEK9, this region is conserved only among terrestrial vertebrates (Figure 41C). NEK8, a close homolog of NEK9 that lacks the corresponding C-terminal region downstream of RCC1-repeats, did not interact with MYH9 (Figure 34B) [69].

To determine whether the LIR and residues 973–979 in NEK9 are required for selective autophagy of MYH9, I expressed the LIR-mutant NEK9 W967A or NEK9 Δ973–979 in *Nek9*-KO MEFs. Whereas the expression of wild-type NEK9 abolished the accumulation of MYH9 in *Nek9*-KO MEFs, the expression of NEK9 W967A or NEK9 Δ973–979 did not (Figure 42). Thus, both the LIR and residues 973–979 in NEK9 are essential for mediating selective autophagy of MYH9.

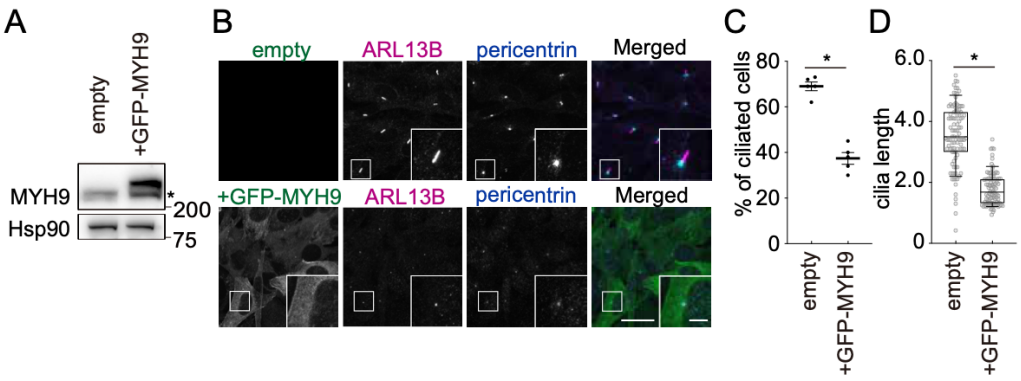

Figure 40. Overexpression of MYH9 inhibits ciliogenesis

(A) Immunoblotting of wild-type MEFs stably expressing empty-vector or GFP-MYH9. The asterisk indicates endogenous MYH9.

(B) Immunofluorescence microscopy of wild-type MEFs stably expressing empty-vector or GFP-MYH9 after serum starvation (24 h). Scale bars, 10 μm and 3 μm (insets).

(C) Frequency of ciliated cells in **(B)**. Data represent the mean ± SEM of five independent experiments (300 cells were counted in each experiment).

(D) Quantification of cilia length in **(B)**. Data were collected from 100 ciliated cells for each cell-type. Solid bars indicate the medians, boxes the interquartile range (25th to 75th percentile), and whiskers the 10th to 90th percentile. *p*-values correspond to two-tailed Mann–Whitney tests; *$p < 0.0001$.

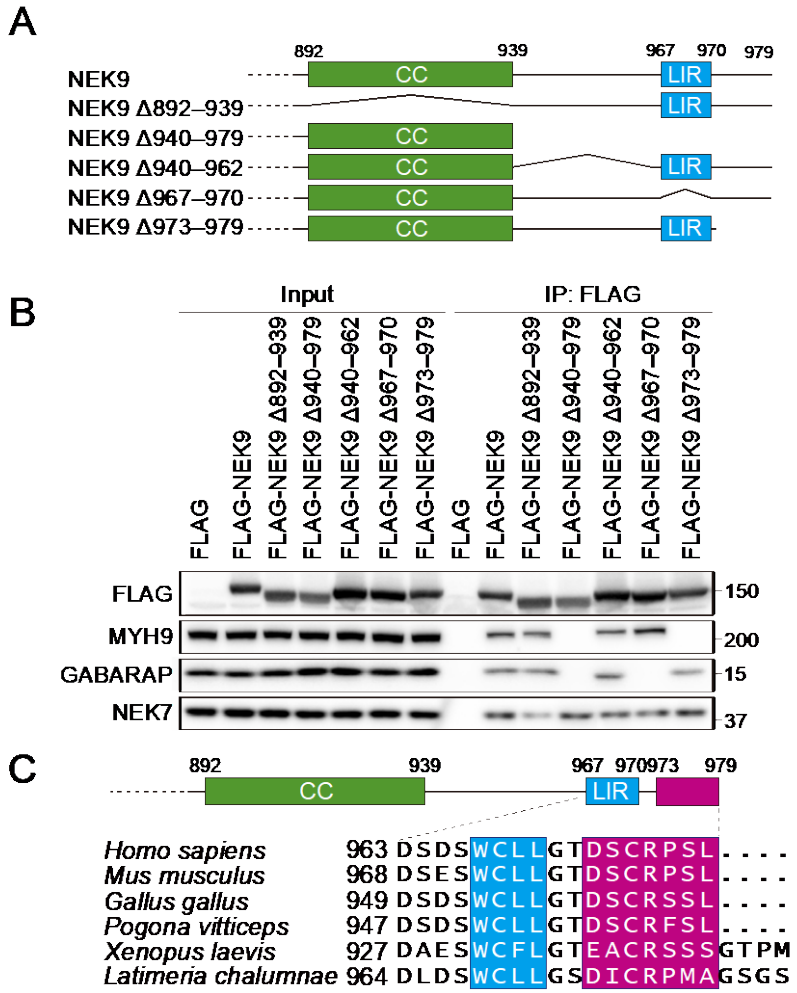

Figure 41. The residues 973-979 in NEK9 is important for binding to MYH9

(A) Schematic representation of the C-terminal regions of *Homo sapiens* NEK9 and deletion mutants. CC, coiled-coil.

(B) Immunoprecipitation using MEFs stably expressing wild-type or deletion mutation NEK9 constructs after serum starvation (4 h). Data are representative of three independent experiments.

(C) Multiple sequence alignment of the C-terminal region of NEK9 from terrestrial vertebrates. The putative MYH9-binding region is colored in magenta.

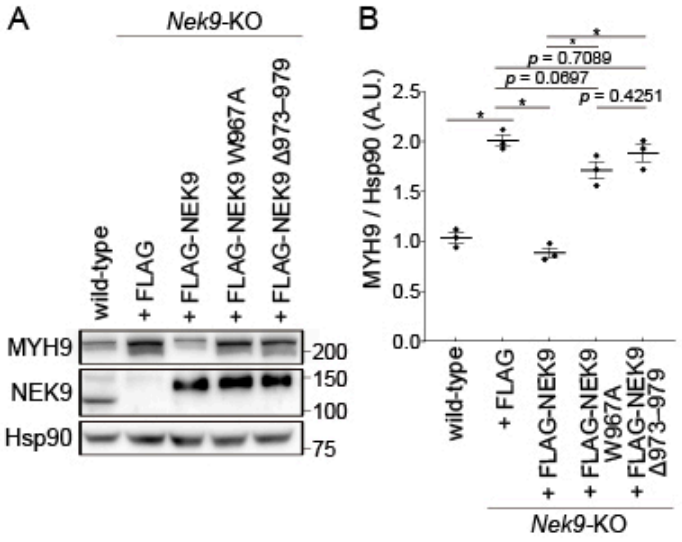

Figure 42. The residues 973–979 in NEK9 are essential for mediating selective autophagy of MYH9

(A) Immunoblotting of wild-type or *Nek9*-KO MEFs stably expressing indicated constructs.

(B) Quantification of the intensity of the MYH9 bands in **(A)**. Data represent the mean ± SEM of three independent experiments. *p*-values correspond to a Tukey's multiple comparisons test; **p* < 0.0001.

Accordingly, the expression of wild-type NEK9 recovered ciliogenesis in *Nek9*-KO MEFs, but that of NEK9 Δ973–979 did not (Figure 43). Thus, NEK9-mediated selective autophagy of MYH9 is required for primary cilia formation.

To rule out the possibility that NEK9 regulates ciliogenesis by binding to proteins other than MYH9, I observed the effect of MYH9 depletion on *Nek9*^{W967A} cells. Short hairpin RNA (shRNA)-mediated knockdown suppressed MYH9 expression in *Nek9*^{W967A} cells to the level observed in serum-starved wild-type cells (Figure 44). In these cells, the defect in ciliogenesis was completely restored (Figure 45), suggesting that NEK9 regulates ciliogenesis by degrading MYH9.

Selective autophagy of MYH9 promotes ciliogenesis by increasing actin dynamics.

Given that MYH9 suppresses actin dynamics by stabilizing the actin filament network [66], I monitored actin dynamics in *Nek9*^{W967A} cells by fluorescence recovery after photobleaching (FRAP) analysis. The fluorescence recovery of GFP-actin after photobleaching was delayed in *Nek9*^{W967A} cells compared to wild-type cells (Figure 46) and was completely restored by knockdown of MYH9, suggesting that actin dynamics are impaired by the accumulation of MYH9 in *Nek9*^{W967A} cells. Thus, selective autophagy of MYH9 via NEK9 promotes ciliogenesis by increasing actin dynamics.

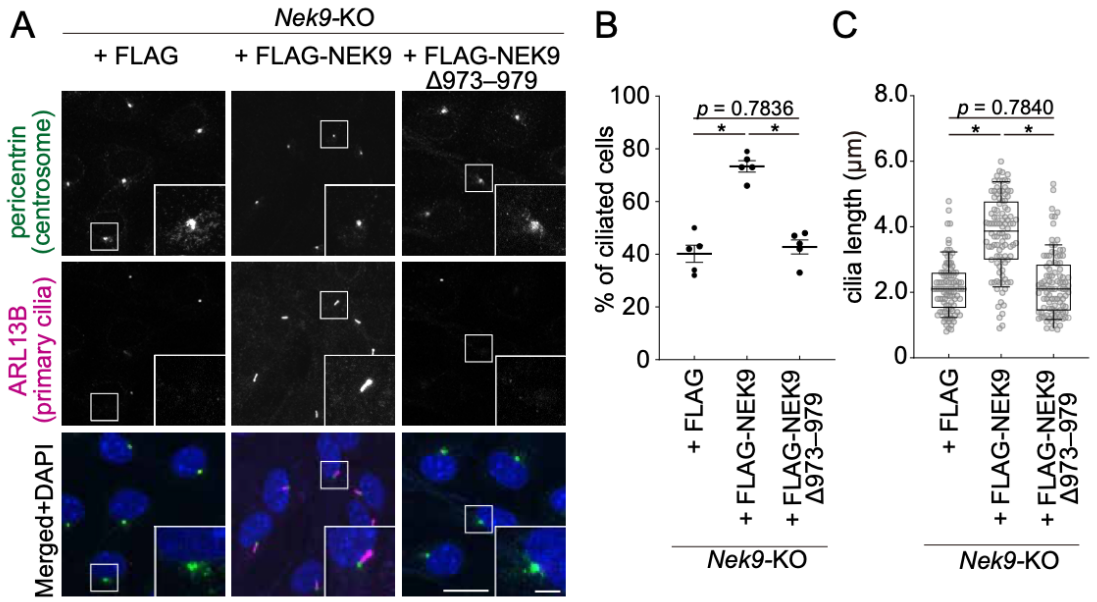

Figure 43. NEK9-mediated selective autophagy of MYH9 is required for primary cilia formation

(A) Immunofluorescence microscopy of *Nek9*-KO MEFs stably expressing indicated constructs after serum starvation (24 h).

(B) Frequency of ciliated cells in **(A)**. Data represent the mean ± SEM of five independent experiments (300 cells were counted in each experiment).

(C) Quantification of cilia length in **(A)**. Data were collected from 100 ciliated cells for each cell-type. Solid bars indicate the medians, boxes the interquartile range (25th to 75th percentile), and whiskers the 10th to 90th percentile. *p*-values correspond to a Tukey's multiple comparisons test; *$p < 0.0001$.

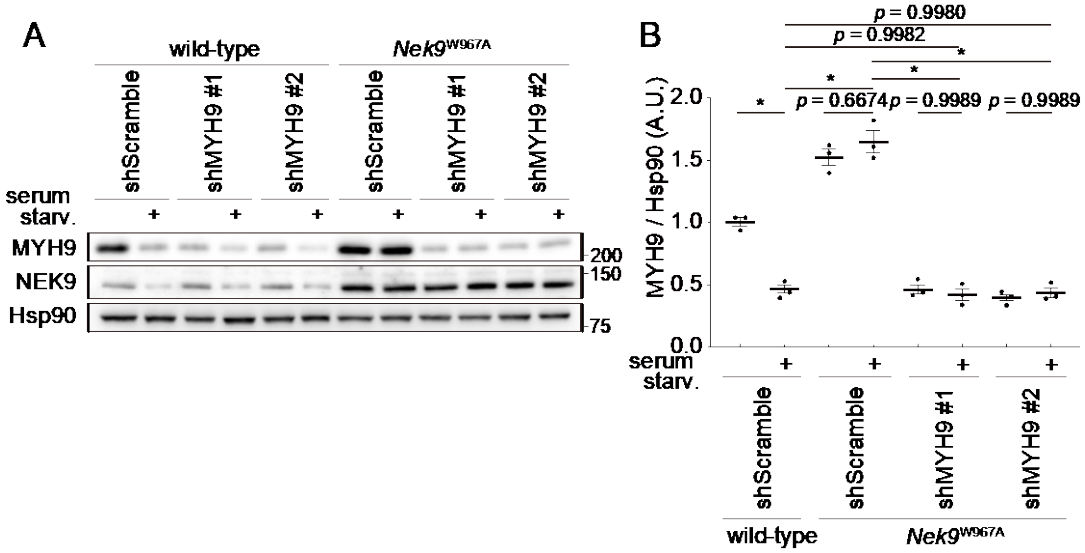

Figure 44. shRNA-mediated knockdown suppressed MYH9 expression in *Nek9*^{W967A} cells to the level observed in serum-starved wild-type cells

(A) Immunoblotting of wild-type or *Nek9*^{W967A} MEFs in which MYH9 was depleted by shRNA-mediated knockdown.

(**B)** Quantification of the intensity of the MYH9 bands in **(A)**. Data represent the mean ± SEM of three independent experiments. *p*-values correspond to a Tukey's multiple comparisons test; *$p < 0.0001$.

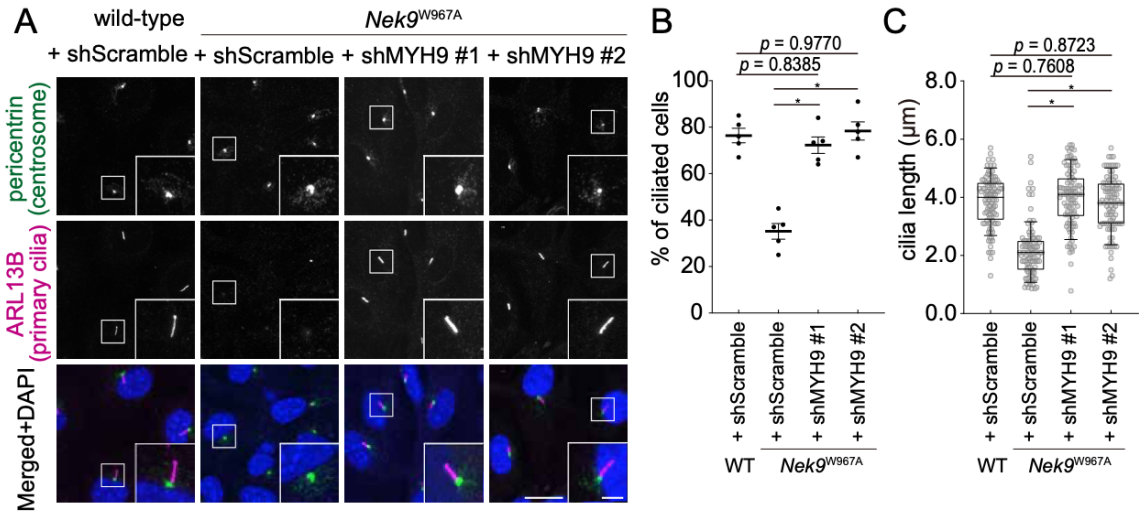

Figure 45. NEK9 regulates ciliogenesis by degrading MYH9

(A) Immunofluorescence microscopy of *Nek9*^{W967A} MEFs in which MYH9 was depleted by two independent shRNAs (#1 and #2). Scale bars, 10 µm and 3 µm (insets).

(B) Frequency of ciliated cells in **(A)**. Data represent the mean ± SEM of five independent experiments (300 cells were counted in each experiment).

(C) Quantification of cilia length in **(A)**. Data were collected from 100 ciliated cells for each cell-type. Solid bars indicate the medians, boxes the interquartile range (25th to 75th percentile), and whiskers the 10th to 90th percentile. *p*-values correspond to a Tukey's multiple comparisons test; *$p < 0.0001$.

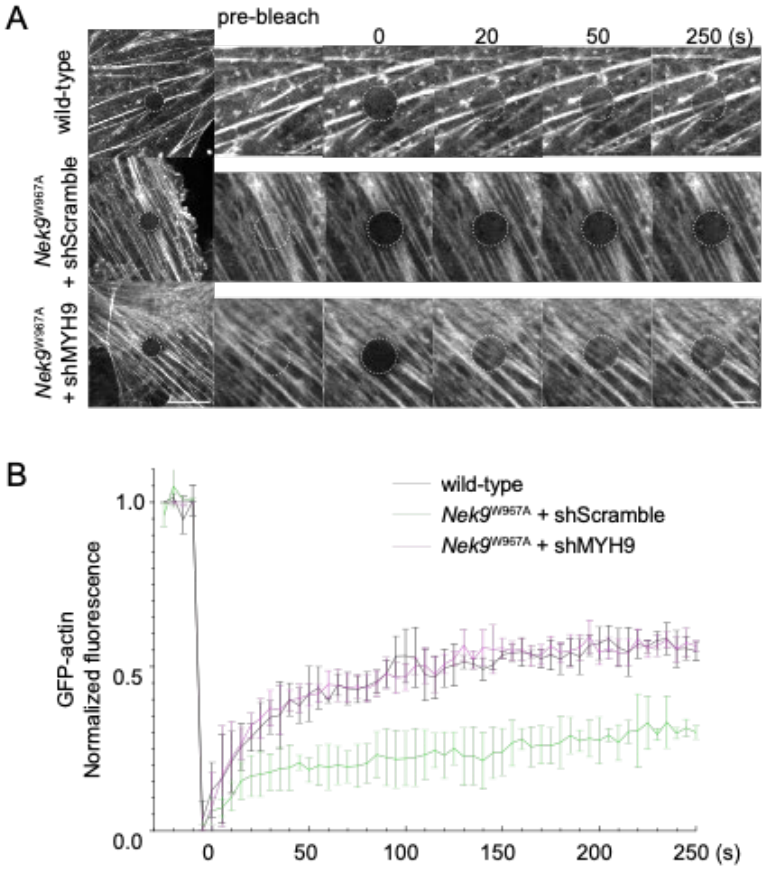

Figure 46. Selective autophagy of MYH9 promotes ciliogenesis by increasing actin dynamics

(A) FRAP analysis of GFP-actin in wild-type or *Nek9*^{W967A} MEFs after serum starvation (24 h). MYH9 was depleted by shRNA-mediated knockdown (#1). Images were recorded at 5-s intervals following photobleaching of the indicated area. Scale bars, 10 μm and 3 μm (insets).

(B) Fluorescence recovery at different time points was quantified. Data represent the mean ± SEM of 10 cells. Similar results were obtained using shMYH9 #2 (not shown). The knockdown efficiency is shown in Figure 44.

Autophagic degradation of NEK9–MYH9 and OFD1 is required for primary cilia formation.

OFD1 at centriolar satellites is a negative regulator of ciliogenesis and was previously shown to be degraded by autophagy [27]. I confirmed that OFD1 at centriolar satellites was degraded under serum starvation conditions, and this degradation was suppressed in *Fip200*-KO cells (Figure 47, 48). Furthermore, in OFD1-overexpressing cells, OFD1 accumulated at centriolar satellites, even under serum starvation conditions, and primary cilia formation was impaired (Figure 49). Thus, OFD1 at centriolar satellites is indeed a negative regulator of ciliogenesis and undergoes autophagy-dependent degradation.

Next, I examined the relationship between NEK9–MYH9 and OFD1. OFD1 did not interact with NEK9 or MYH9 (Figure 50). Whereas OFD1-overexpressing cells showed normal actin dynamics (Figure 51), OFD1 accumulated at centriolar satellites in *Nek9*^{W967A} cells (Figure 52, 53), suggesting that NEK9 regulates the degradation or dynamics of OFD1. However, although knockdown of OFD1 depleted OFD1 at centriolar satellites, it did not restore the defect in ciliogenesis in *Nek9*^{W967A} cells (Figure 52, 53), indicating that OFD1 accumulation is not the major cause of the impaired ciliogenesis in *Nek9*^{W967A} cells. In contrast, MYH9 knockdown depleted

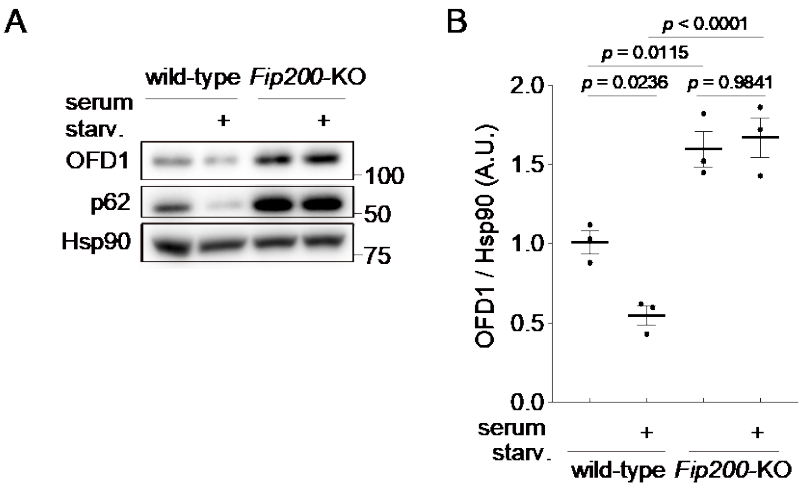

Figure 47. OFD1 is degraded by autophagy

(A) Immunoblotting of wild-type and *Fip200*-KO MEFs under nutrient-rich conditions or after serum starvation (24 h).

(B) Quantification of the intensity of the OFD1 bands in **(A)**. Data represent the mean ± SEM of three independent experiments. *p*-values correspond to Tukey's multiple comparisons tests.

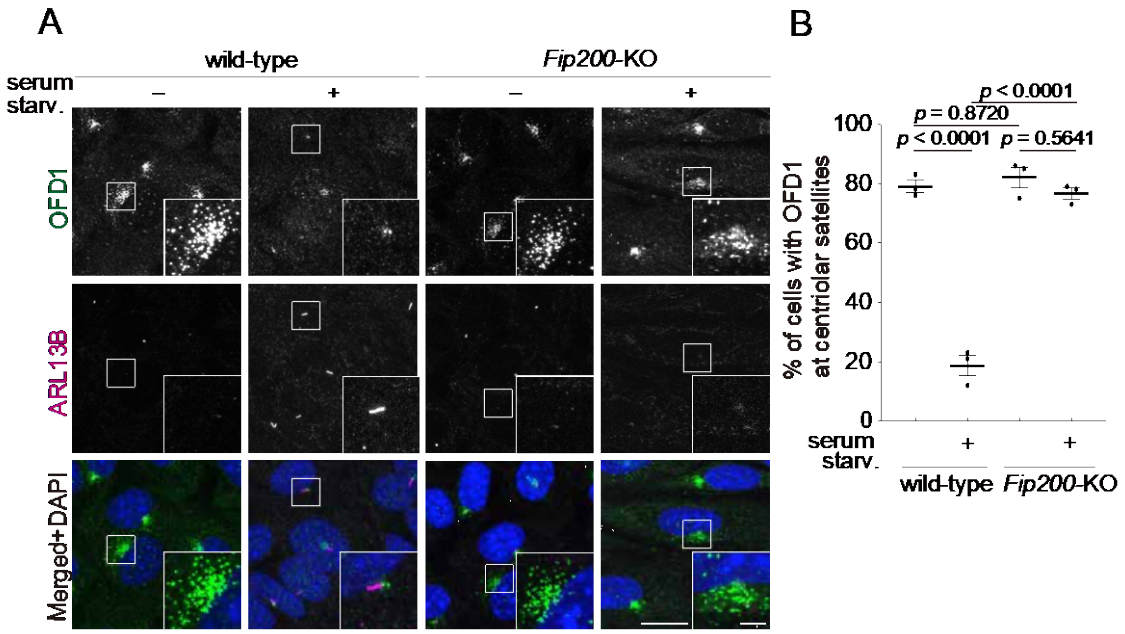

Figure 48. OFD1 at centriolar satellites is degraded by autophagy

(A) Immunofluorescence microscopy of wild-type and *Fip200*-KO MEFs under nutrient-rich conditions or after serum starvation (24 h). Scale bars, 10 μm and 3 μm (insets). **(B)** Percentage of cells with centriolar satellites OFD1 in **(A)**. Data represent the mean ± SEM of three independent experiments (100 cells were counted in each experiment). *p*-values correspond to Tukey's multiple comparisons tests.

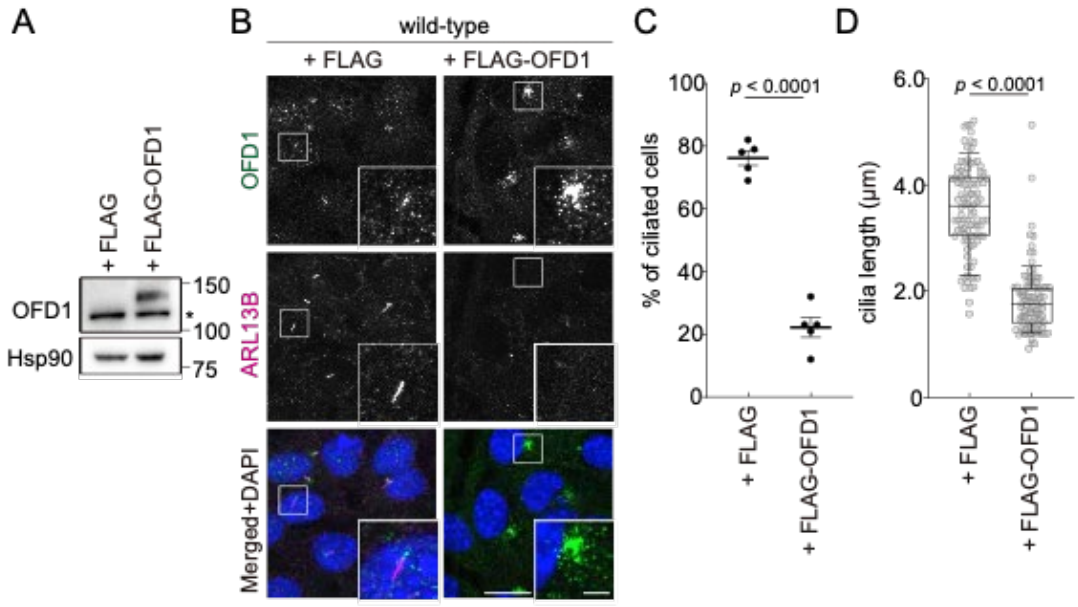

Figure 49. OFD1 at centriolar satellites is a negative regulator of ciliogenesis

(A) Immunoblotting of wild-type MEFs stably expressing FLAG or FLAG-OFD1. The asterisk indicates endogenous OFD1.

(B) Immunofluorescence microscopy of wild-type MEFs stably expressing FLAG or FLAG-OFD1 after serum starvation (24 h). Scale bars, 10 µm and 3 µm (insets).

(C) Frequency of ciliated cells in **(B)**. Data represent the mean ± SEM of five independent experiments (300 cells were counted in each experiment).

(D) Quantification of cilia length in **(B)**. Data were collected from 100 ciliated cells for each cell-type. Solid bars indicate the medians, boxes the interquartile range (25th to 75th percentile), and whiskers the 10th to 90th percentile. *p*-values correspond to two-tailed Mann–Whitney tests.

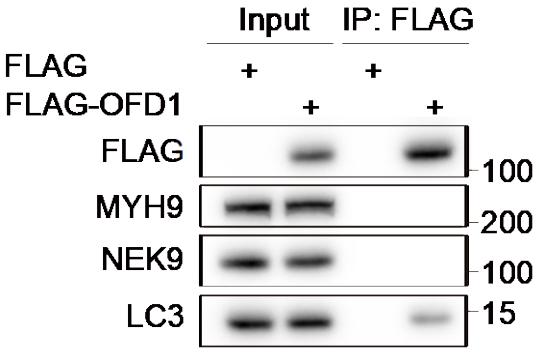

Figure 50. OFD1 does not interact with NEK9 or MYH9

Immunoprecipitation using MEFs stably expressing FLAG or FLAG-OFD1. Data are representative of three independent experiments.

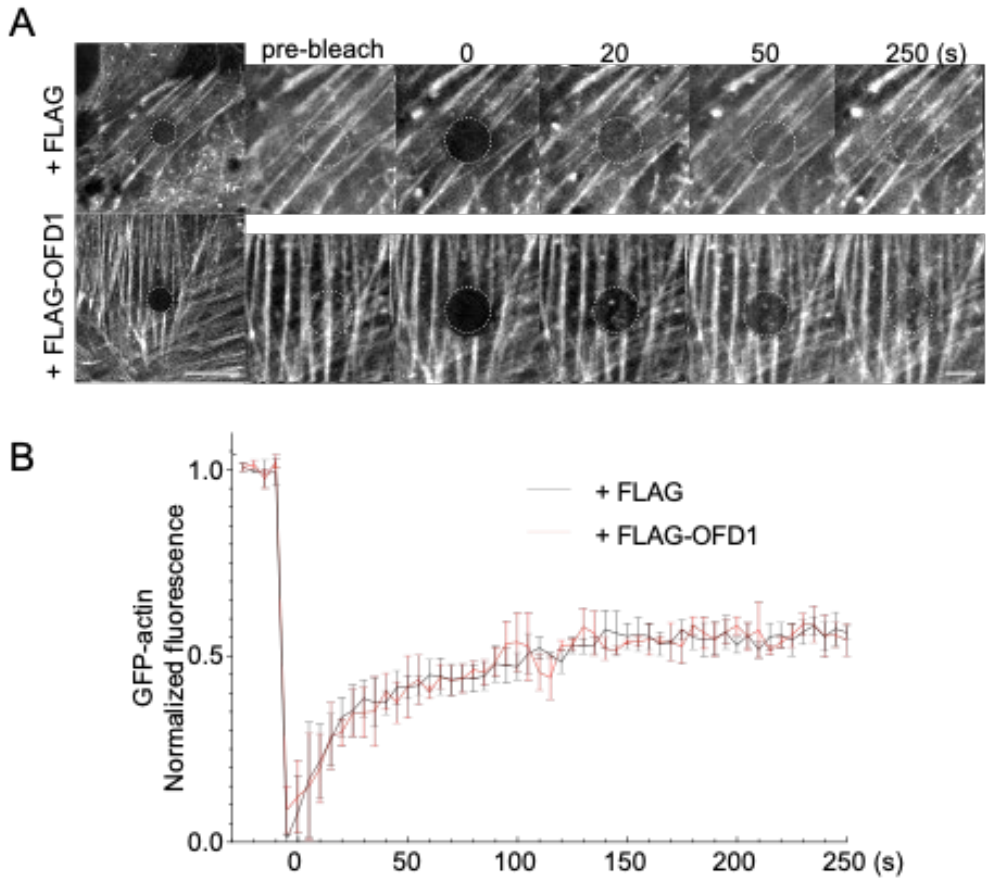

Figure 51. Overexpression of OFD1 does not affect actin dynamics

(A) FRAP analysis of GFP-actin in wild-type MEFs stably expressing FLAG or FLAG-OFD1 after serum starvation (24 h). Images were recorded at 5-s intervals following photobleaching of the indicated area.

(B) Fluorescence recovery at different time points was quantified. Data represent the mean ± SEM of 10 cells.

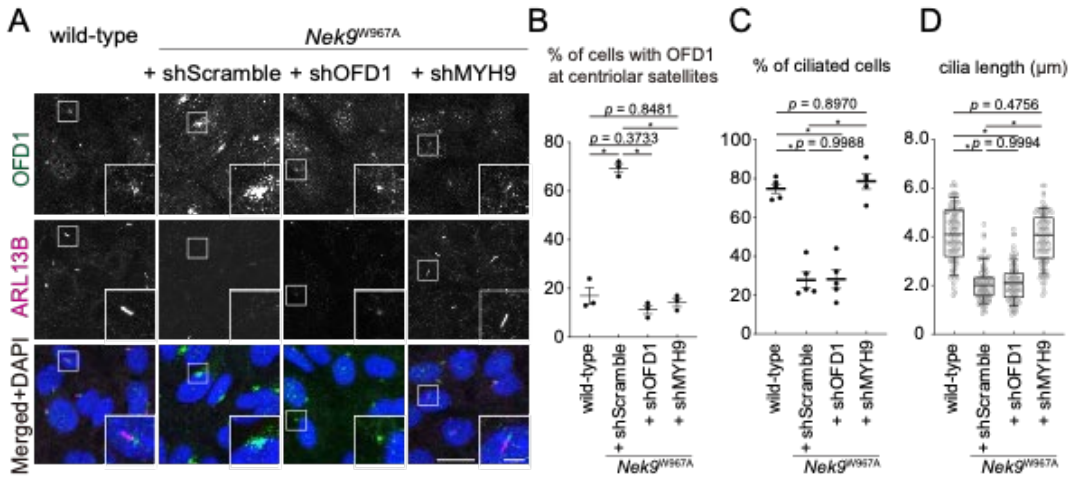

Figure 52. NEK9–MYH9 and OFD1 inhibit ciliogenesis at different steps

(A) Immunofluorescence microscopy of wild-type or *Nek9*^{W967A} MEFs after serum starvation (24 h). OFD1 or MYH9 was depleted by shRNA-mediated knockdown (shMYH9 #1 was used). Similar results were obtained using shMYH9 #2 and two independent shOFD1 (not shown). Scale bars, 10 µm and 3 µm (insets).

(B) Percentage of cells with centriolar satellites OFD1 in **(A)**. Data represent the mean ± SEM of three independent experiments (100 cells were counted in each experiment).

(C) Frequency of ciliated cells in **(A)**. Data represent the mean ± SEM of five independent experiments (300 cells were counted in each experiment).

(D) Quantification of cilia length in **(A)**. Data were collected from 100 ciliated cells for each cell-type. *p*-values correspond to a Tukey's multiple comparisons test; **p* < 0.0001.

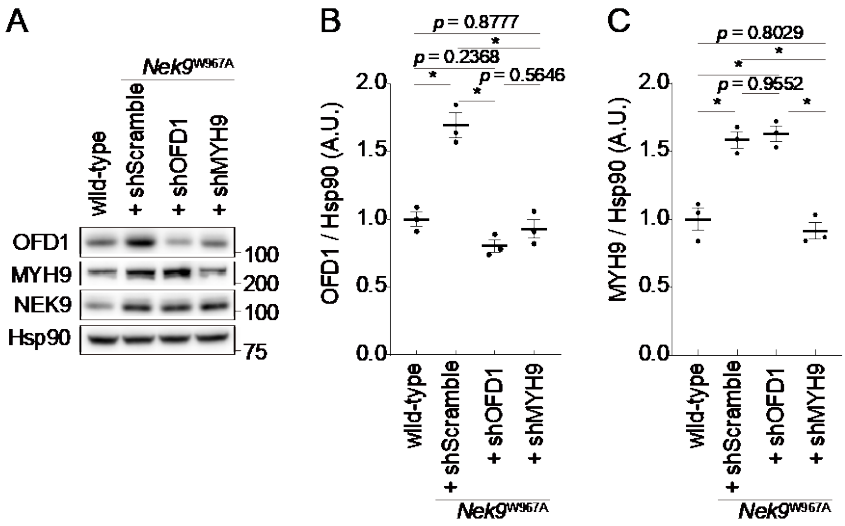

Figure 53. OFD1 degradation indirectly depends on MYH9 degradation

(A) Immunoblotting of wild-type and *Nek9*^{W967A} MEFs after serum starvation (24 h). OFD1 or MYH9 was depleted by shRNA-mediated knockdown.

(B) Quantification of the intensity of the OFD1 bands in **(A)**.

(C) Quantification of the intensity of the MYH9 bands in **(A)**. Data represent the mean ± SEM of three independent experiments. *p*-values correspond to Tukey's multiple comparisons tests; **p* < 0.0001.

OFD1 at centriolar satellites and recovered ciliogenesis. These data suggest that, although the degradation of OFD1 depends on MYH9 degradation, it seems to be an indirect effect and that NEK9–MYH9 and OFD1 inhibit ciliogenesis at different steps.

Finally, I determined the contribution of autophagy-dependent degradation of MYH9 and OFD1 to ciliogenesis by depleting MYH9 and/or OFD1 in autophagy-deficient *Fip200*-KO MEFs. Although shMYH9 and shOFD1 suppressed the expression of these proteins to levels observed in serum-starved wild-type cells (Figure 54), single knockdown of MYH9 or OFD1 only partially rescued the defect in ciliogenesis. In contrast, knockdown of both MYH9 and OFD1 completely restored the defect (Figure 55), further indicating the indirect relationship between MYH9 and OFD1. These data suggest that the autophagic degradation of both MYH9 and OFD1 is important for ciliogenesis and that autophagy drives primary cilia formation at least at two distinct steps (Figure 56).

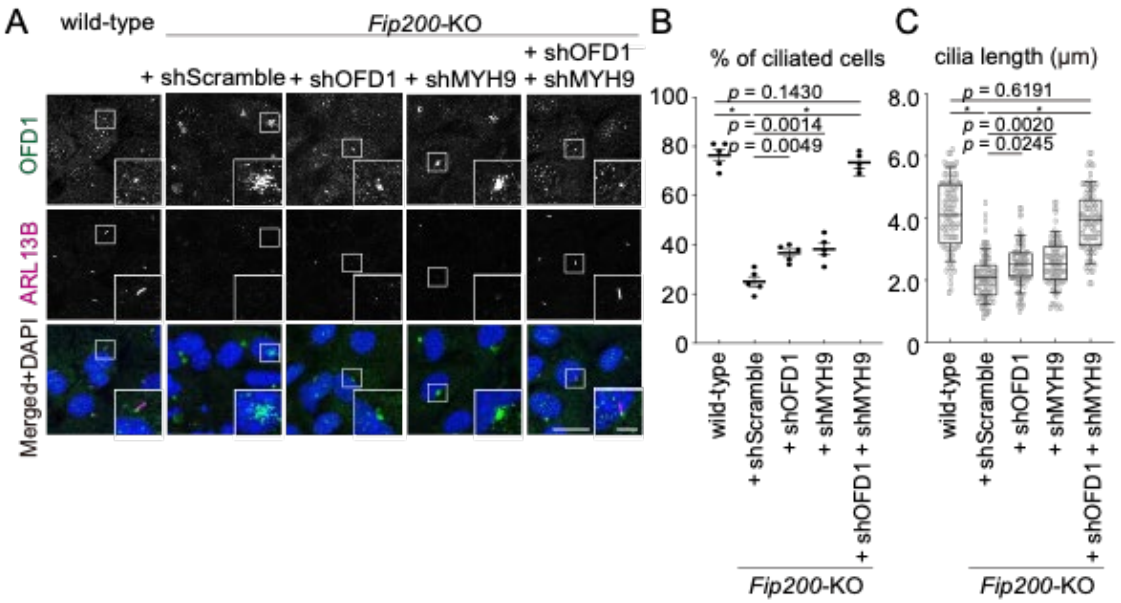

Figure 54. Autophagic degradation of NEK9–MYH9 and OFD1 is required for primary cilia formation

(A) Immunofluorescence microscopy of wild-type or *Fip200*-KO MEFs after serum starvation (24 h). OFD1 and/or MYH9 were depleted by shRNA-mediated knockdown. Scale bars, 10 µm and 3 µm (insets).

(B) Frequency of ciliated cells in **(A)**. Data represent the mean ± SEM of five independent experiments (300 cells were counted in each experiment).

(C) Quantification of cilia length in **(A)**. Data were collected from 100 ciliated cells for each cell-type. Solid bars indicate the medians, boxes the interquartile range (25th to 75th percentile), and whiskers the 10th to 90th percentile. *p*-values correspond to a Tukey's multiple comparisons test; *$p < 0.0001$.

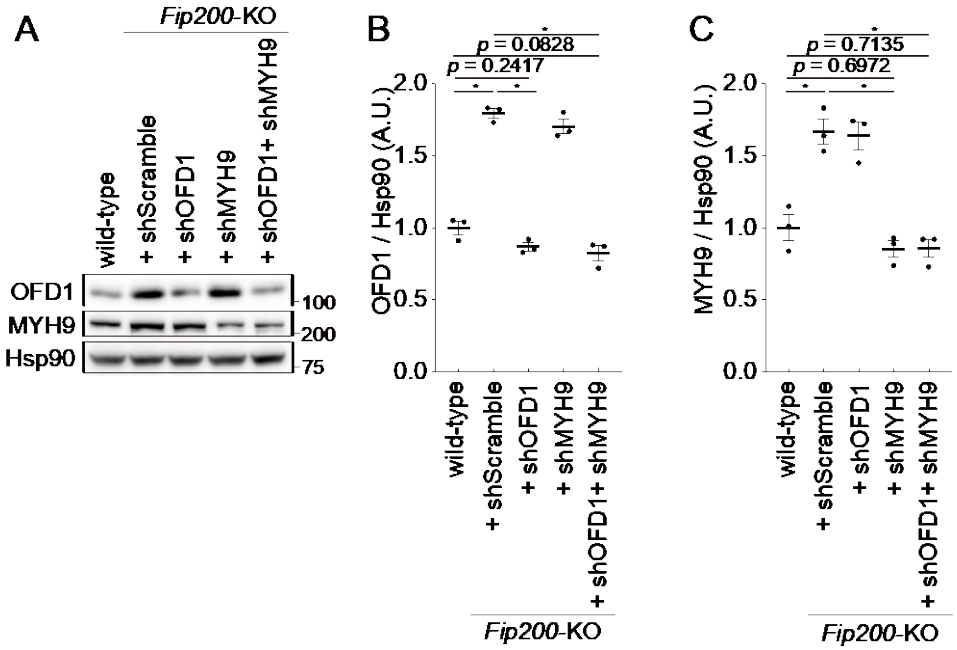

Figure 55. Autophagic degradation of NEK9–MYH9 and OFD1 is required for primary cilia formation

(A) Immunoblotting of wild-type and *Fip200-KO* MEFs after serum starvation (24 h). OFD1 and/or MYH9 were depleted by shRNA-mediated knockdown.

(B) Quantification of the intensity of the OFD1 bands in **(A)**.

(C) Quantification of the intensity of the MYH9 bands in **(A)**. Data represent the mean ± SEM of three independent experiments. *p*-values correspond to Tukey's multiple comparisons tests; *$p < 0.0001$.

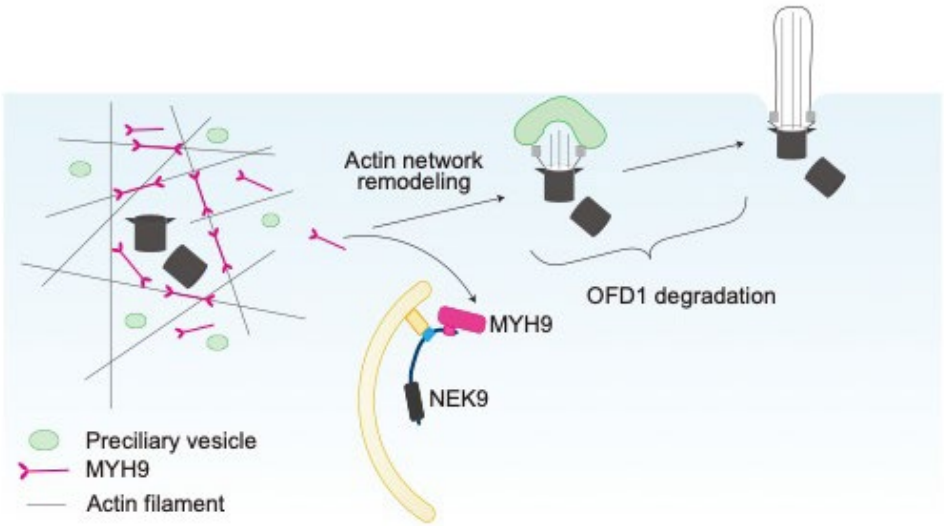

Figure 56. Model of how autophagy drives primary cilia formation

The autophagic degradation of both MYH9 and OFD1 is important for ciliogenesis. Autophagy drives primary cilia formation at least at two distinct steps

Discussion

Autophagy regulates primary cilia formation, but the underlying mechanism is not fully understood. In this study, I showed that NEK9 functions as a selective autophagy adaptor to degrade MYH9 and promotes ciliogenesis by increasing actin dynamics. The antagonistic activity between MYH9 and MYH10 indicates that the regulation of relative amounts of these proteins is important for ciliogenesis, but the underlying mechanism has remained largely unknown [66]. My results suggest that selective autophagy decreases the relative amount of MYH9 to MYH10 and promotes ciliogenesis. The LIR and the putative MYH9 binding region (residues 973–979) of NEK9 are in close proximity. Given that regions around the core LIR could also be involved in interaction with ATG8s, this proximity may prevent NEK9 from binding to both ATG8s and MYH9 at the same time (Figure 41) [12, 70]. One possible explanation is that NEK9 forms a dimer through the coiled-coil region [37,41] and binds to MYH9 and ATG8s *in trans*.

My data suggest that, although autophagic degradation of both NEK9–MYH9 and OFD1 is essential, the degradation of OFD1 may be partially dependent on that of NEK9–MYH9. Actin network remodeling preceding ciliogenesis allows other organelles, including RAB11-positive recycling endosomes, access to the vicinity of centriolar

satellites. Thus, although autophagic degradation of NEK9–MYH9 and OFD1 seems to promote ciliogenesis at different steps, it is possible that increased actin dynamics by selective autophagy of MYH9 indirectly facilitates the degradation of OFD1 at centriolar satellites [56].

This study is consistent with a previous report that NEK9 could be a causative gene of ciliopathies [46]. Lethal skeletal dysplasia and impaired ciliogenesis were observed in a patient with a nonsense mutation (c.1489C>T; p.Arg497*) in *NEK9*. No NEK9 protein was detected in patient fibroblasts, indicating both the kinase activity and autophagy adaptor function were lost [46]. Whereas skeletal dysplasia is widely accepted as a common feature of ciliopathy, *Nek9*$^{W967A/W967A}$ mice exhibited no skeletal abnormalities, despite showing a defect in ciliogenesis. Therefore, the skeletal dysplasia observed in NEK9-related diseases is probably due to mitotic dysregulation resulting from the loss of NEK9 kinase activity, rather than impaired ciliogenesis.

Human NEK family consists of 11 NEK proteins from NEK1 to NEK11, which distinctly share an N-terminal catalytic kinase domain. Other NEK proteins, such as NEK1 and NEK8, are also involved in ciliogenesis [37]. However, the NEK9 sequence containing the LIR and potential MYH9-binding site are not conserved in any other NEK proteins including NEK1 and NEK8. Rather, NEK9 seems to evolutionary acquire these

regions in a limited branch of vertebrates. In addition to that, the expression levels are not consistent among NEK family proteins [37]. Considering these differences in protein structure and expression profile among NEK family proteins, it seems unlikely that other family proteins could substitute the function of NEK9. Rather, NEK1 and NEK8 localize directly to the basal body and cilia to promote cilia formation depending on their kinase activity (at least for NEK8) [69]. This is in sharp contrast to the case of NEK9, which promotes ciliogenesis without localizing to these organelles in a kinase-activity-independent manner (Figure 24).

Our results suggest that NEK9 functions not only as an essential kinase for mitosis progression, but also as a selective autophagy adaptor important for ciliogenesis, which occurs in interphase. Many proteins have been reported to exert different functions in mitosis and interphase, and some of them have acquired the second function through evolution [86]. In the case of NEK9, the LIR and MYH9 binding region were acquired during the evolution of terrestrial vertebrates, suggesting that NEK9 acquired the second function related to autophagy and ciliogenesis at this stage.

It has been reported that phosphorylation can act as a molecular switch to change the function of proteins between mitosis and interphase [86, 87]. In the case of NEK9, when the cell enters mitosis, upstream kinase like CDK1 phosphorylates the serine

residues in kinase domain of NEK9 [37], allowing it to auto-dimerize and exert its mitotic function and possibly inhibiting its autophagy-related function; dimerization by coiled-coil region nearby the LIR may structurally inhibit LC3/GABARAP to interact with LIR.

In addition to that, phosphorylation of serine/threonine residues around LIR has been reported to regulate the activity of selective autophagy by changing the binding affinity between LC3/GABARAP and LIR [12]. Since NEK9 possesses conserved serine/threonine residues around LIR (Figure 5), phosphorylation of them could be another regulatory mechanism to switch its dual functions between mitosis and interphase.

A dramatic functional evolution occurred in the vertebrate kidney during the fish-to-tetrapod transition to overcome physiological changes [71], including acquisition of the ability to excrete nitrogen or maintain homeostasis of water and various small molecules. During this evolution, the vertebrate kidney acquired primary cilia; in contrast to primary cilia found in the kidneys of higher vertebrates, all cilia in fish kidneys are motile [72,73]. Therefore, I speculate that the evolutionary acquisition of the LIR of NEK9 was critical for the newly-acquired primary cilia formation in the tetrapod kidney and thus for the adaptation of vertebrates to terrestrial habitats.

References

1. Malicki, J.J. & Johnson, C.A. The Cilium: Cellular Antenna and Central Processing Unit. *Trends Cell Biol* **27**, 126-140 (2017).

2. Anvarian, Z., Mykytyn, K., Mukhopadhyay, S., Pedersen, L.B. & Christensen, S.T. Cellular signalling by primary cilia in development, organ function and disease. *Nat Rev Nephrol* **15**, 199-219 (2019).

3. Spasic, M. & Jacobs, C.R. Primary cilia: Cell and molecular mechanosensors directing whole tissue function. *Semin Cell Dev Biol* **71**, 42-52 (2017).

4. Berbari, N.F., O'Connor, A.K., Haycraft, C.J. & Yoder, B.K. The primary cilium as a complex signaling center. *Curr Biol* **19**, R526-535 (2009).

5. Tummala, P., Arnsdorf, E.J. & Jacobs, C.R. The Role of Primary Cilia in Mesenchymal Stem Cell Differentiation: A Pivotal Switch in Guiding Lineage Commitment. *Cell Mol Bioeng* **3**, 207-212 (2010).

6. Wheway, G., Nazlamova, L. & Hancock, J.T. Signaling through the Primary Cilium. *Front Cell Dev Biol* **6**, 8 (2018).

7. Reiter, J.F. & Leroux, M.R. Genes and molecular pathways underpinning ciliopathies. *Nat Rev Mol Cell Biol* **18**, 533-547 (2017).

8. Hildebrandt, F., Benzing, T. & Katsanis, N. Ciliopathies. *N Engl J Med* **364**, 1533-1543 (2011).

9. Nakatogawa, H. Mechanisms governing autophagosome biogenesis. *Nat Rev Mol Cell Biol* **21**, 439-458 (2020).

10. Soreng, K., Neufeld, T.P. & Simonsen, A. Membrane Trafficking in Autophagy. *Int Rev Cell Mol Biol* **336**, 1-92 (2018).

11. Gatica, D., Lahiri, V. & Klionsky, D.J. Cargo recognition and degradation by selective autophagy. *Nat Cell Biol* **20**, 233-242 (2018).

12. Johansen, T. & Lamark, T. Selective Autophagy: ATG8 Family Proteins, LIR Motifs and Cargo Receptors. *J Mol Biol* **432**, 80-103 (2020).

13. Gomes, L.C. & Dikic, I. Autophagy in antimicrobial immunity. *Mol Cell* **54**, 224-233 (2014).

14. Palikaras, K., Lionaki, E. & Tavernarakis, N. Mechanisms of mitophagy in cellular homeostasis, physiology and pathology. *Nat Cell Biol* **20**, 1013-1022 (2018).

15. Chino, H. & Mizushima, N. ER-Phagy: Quality Control and Turnover of Endoplasmic Reticulum. *Trends Cell Biol* **30**, 384-398 (2020).

16. Anding, A.L. & Baehrecke, E.H. Cleaning House: Selective Autophagy of

Organelles. *Dev Cell* **41**, 10-22 (2017).

17. Dikic, I. & Elazar, Z. Mechanism and medical implications of mammalian autophagy. *Nat Rev Mol Cell Biol* **19**, 349-364 (2018).

18. Mizushima, N., Levine, B. Autophagy in human diseases. *N. Engl. J. Med. in press*

19. Mizushima, N. The ATG conjugation systems in autophagy. *Curr Opin Cell Biol* **63**, 1-10 (2020).

20. Birgisdottir, A.B., Lamark, T. & Johansen, T. The LIR motif - crucial for selective autophagy. *J Cell Sci* **126**, 3237-3247 (2013).

21. Morleo, M. & Franco, B. The Autophagy-Cilia Axis: An Intricate Relationship. *Cells* **8** (2019).

22. Pampliega, O. & Cuervo, A.M. Autophagy and primary cilia: dual interplay. *Curr Opin Cell Biol* **39**, 1-7 (2016).

23. Odabasi, E., Gul, S., Kavakli, I.H. & Firat-Karalar, E.N. Centriolar satellites are required for efficient ciliogenesis and ciliary content regulation. *EMBO Rep* **20** (2019).

24. Prosser, S.L. & Pelletier, L. Centriolar satellite biogenesis and function in vertebrate cells. *J Cell Sci* **133** (2020).

25. Ferrante, M.I. *et al.* Oral-facial-digital type I protein is required for primary cilia

formation and left-right axis specification. *Nat Genet* **38**, 112-117 (2006).

26. Singla, V., Romaguera-Ros, M., Garcia-Verdugo, J.M. & Reiter, J.F. Ofd1, a human disease gene, regulates the length and distal structure of centrioles. *Dev Cell* **18**, 410-424 (2010).

27. Tang, Z. *et al.* Autophagy promotes primary ciliogenesis by removing OFD1 from centriolar satellites. *Nature* **502**, 254-257 (2013).

28. Liu, Z.Q. *et al.* Ciliogenesis is reciprocally regulated by PPARA and NR1H4/FXR through controlling autophagy in vitro and in vivo. *Autophagy* **14**, 1011-1027 (2018).

29. Hsiao, C.J. *et al.* Gli2 modulates cell cycle re-entry through autophagy-mediated regulation of the length of primary cilia. *J Cell Sci* **131** (2018).

30. Wang, S., Livingston, M.J., Su, Y. & Dong, Z. Reciprocal regulation of cilia and autophagy via the MTOR and proteasome pathways. *Autophagy* **11**, 607-616 (2015).

31. Kim, E.S. *et al.* Inhibition of autophagy suppresses sertraline-mediated primary ciliogenesis in retinal pigment epithelium cells. *PLoS One* **10**, e0118190 (2015).

32. Pampliega, O. *et al.* Functional interaction between autophagy and ciliogenesis. *Nature* **502**, 194-200 (2013).

33. Struchtrup, A., Wiegering, A., Stork, B., Ruther, U. & Gerhardt, C. The ciliary protein RPGRIP1L governs autophagy independently of its proteasome-regulating function at the ciliary base in mouse embryonic fibroblasts. *Autophagy* **14**, 567-583 (2018).

34. Chino, H., Hatta, T., Natsume, T. & Mizushima, N. Intrinsically Disordered Protein TEX264 Mediates ER-phagy. *Mol Cell* **74**, 909-921 e906 (2019).

35. Joachim, J. *et al.* Centriolar Satellites Control GABARAP Ubiquitination and GABARAP-Mediated Autophagy. *Curr Biol* **27**, 2123-2136 e2127 (2017).

36. Behrends, C., Sowa, M.E., Gygi, S.P. & Harper, J.W. Network organization of the human autophagy system. *Nature* **466**, 68-76 (2010).

37. Fry, A.M., Bayliss, R. & Roig, J. Mitotic Regulation by NEK Kinase Networks. *Front Cell Dev Biol* **5**, 102 (2017).

38. Moniz, L., Dutt, P., Haider, N. & Stambolic, V. Nek family of kinases in cell cycle, checkpoint control and cancer. *Cell Div* **6**, 18 (2011).

39. Cullati, S.N., Kabeche, L., Kettenbach, A.N. & Gerber, S.A. A bifurcated signaling cascade of NIMA-related kinases controls distinct kinesins in anaphase. *J Cell Biol* **216**, 2339-2354 (2017).

40. Eibes, S. *et al.* Nek9 Phosphorylation Defines a New Role for TPX2 in Eg5-

Dependent Centrosome Separation before Nuclear Envelope Breakdown. *Curr Biol* **28**, 121-129 e124 (2018).

41. Roig, J., Mikhailov, A., Belham, C. & Avruch, J. Nercc1, a mammalian NIMA-family kinase, binds the Ran GTPase and regulates mitotic progression. *Genes Dev* **16**, 1640-1658 (2002).

42. Bertran, M.T. *et al.* Nek9 is a Plk1-activated kinase that controls early centrosome separation through Nek6/7 and Eg5. *EMBO J* **30**, 2634-2647 (2011).

43. Upadhya, P., Birkenmeier, E.H., Birkenmeier, C.S. & Barker, J.E. Mutations in a NIMA-related kinase gene, Nek1, cause pleiotropic effects including a progressive polycystic kidney disease in mice. *Proc Natl Acad Sci U S A* **97**, 217-221 (2000).

44. Otto, E.A. *et al.* NEK8 mutations affect ciliary and centrosomal localization and may cause nephronophthisis. *J Am Soc Nephrol* **19**, 587-592 (2008).

45. Chivukula, R.R. *et al.* A human ciliopathy reveals essential functions for NEK10 in airway mucociliary clearance. *Nat Med* **26**, 244-251 (2020).

46. Casey, J.P. *et al.* Recessive NEK9 mutation causes a lethal skeletal dysplasia with evidence of cell cycle and ciliary defects. *Hum Mol Genet* **25**, 1824-1835 (2016).

47. Shrestha, B.K. *et al.* NIMA-related kinase 9-mediated phosphorylation of the

microtubule-associated LC3B protein at Thr-50 suppresses selective autophagy of p62/sequestosome 1. *J Biol Chem* **295**, 1240-1260 (2020).

48. Kalvari, I. *et al.* iLIR: A web resource for prediction of Atg8-family interacting proteins. *Autophagy* **10**, 913-925 (2014).

49. Amemiya, C.T. *et al.* The African coelacanth genome provides insights into tetrapod evolution. *Nature* **496**, 311-316 (2013).

50. Yoshii, S.R. *et al.* Systemic Analysis of Atg5-Null Mice Rescued from Neonatal Lethality by Transgenic ATG5 Expression in Neurons. *Dev Cell* **39**, 116-130 (2016).

51. Natsume, T., Kiyomitsu, T., Saga, Y. & Kanemaki, M.T. Rapid Protein Depletion in Human Cells by Auxin-Inducible Degron Tagging with Short Homology Donors. *Cell Rep* **15**, 210-218 (2016).

52. Boehlke, C. *et al.* Primary cilia regulate mTORC1 activity and cell size through Lkb1. *Nat Cell Biol* **12**, 1115-1122 (2010).

53. Orhon, I. *et al.* Primary-cilium-dependent autophagy controls epithelial cell volume in response to fluid flow. *Nat Cell Biol* **18**, 657-667 (2016).

54. Kimura, T. *et al.* Autophagy protects the proximal tubule from degeneration and acute ischemic injury. *J Am Soc Nephrol* **22**, 902-913 (2011).

55. Pecci, A., Ma, X., Savoia, A. & Adelstein, R.S. MYH9: Structure, functions and role of non-muscle myosin IIA in human disease. *Gene* **664**, 152-167 (2018).

56. Copeland, J. Actin-based regulation of ciliogenesis - The long and the short of it. *Semin Cell Dev Biol* **102**, 132-138 (2020).

57. Wang, L. & Dynlacht, B.D. The regulation of cilium assembly and disassembly in development and disease. *Development* **145** (2018).

58. Kim, J. *et al.* Functional genomic screen for modulators of ciliogenesis and cilium length. *Nature* **464**, 1048-1051 (2010).

59. Pitaval, A. *et al.* Microtubule stabilization drives 3D centrosome migration to initiate primary ciliogenesis. *J Cell Biol* **216**, 3713-3728 (2017).

60. Cao, J. *et al.* miR-129-3p controls cilia assembly by regulating CP110 and actin dynamics. *Nat Cell Biol* **14**, 697-706 (2012).

61. Kim, J. *et al.* Actin remodelling factors control ciliogenesis by regulating YAP/TAZ activity and vesicle trafficking. *Nat Commun* **6**, 6781 (2015).

62. Yan, X. & Zhu, X. Branched F-actin as a negative regulator of cilia formation. *Exp Cell Res* **319**, 147-151 (2013).

63. Shutova, M.S. & Svitkina, T.M. Mammalian nonmuscle myosin II comes in three flavors. *Biochem Biophys Res Commun* **506**, 394-402 (2018).

64. Even-Ram, S. *et al.* Myosin IIA regulates cell motility and actomyosin-microtubule crosstalk. *Nat Cell Biol* **9**, 299-309 (2007).

65. Vicente-Manzanares, M., Ma, X., Adelstein, R.S. & Horwitz, A.R. Non-muscle myosin II takes centre stage in cell adhesion and migration. *Nat Rev Mol Cell Biol* **10**, 778-790 (2009).

66. Rao, Y., Hao, R., Wang, B. & Yao, T.P. A Mec17-Myosin II Effector Axis Coordinates Microtubule Acetylation and Actin Dynamics to Control Primary Cilium Biogenesis. *PLoS One* **9**, e114087 (2014).

67. Hong, H., Kim, J. & Kim, J. Myosin heavy chain 10 (MYH10) is required for centriole migration during the biogenesis of primary cilia. *Biochem Biophys Res Commun* **461**, 180-185 (2015).

68. Uhlen, M. *et al.* Proteomics. Tissue-based map of the human proteome. *Science* **347**, 1260419 (2015).

69. Fry, A.M., O'Regan, L., Sabir, S.R. & Bayliss, R. Cell cycle regulation by the NEK family of protein kinases. *J Cell Sci* **125**, 4423-4433 (2012).

70. Wirth, M. *et al.* Molecular determinants regulating selective binding of autophagy adapters and receptors to ATG8 proteins. *Nat Commun* **10**, 2055 (2019).

71. Finn, R.N., Chauvigne, F., Hlidberg, J.B., Cutler, C.P. & Cerda, J. The lineage-

specific evolution of aquaporin gene clusters facilitated tetrapod terrestrial adaptation. *PLoS One* **9**, e113686 (2014).

72. Marra, A.N., Li, Y. & Wingert, R.A. Antennas of organ morphogenesis: the roles of cilia in vertebrate kidney development. *Genesis* **54**, 457-469 (2016).

73. Kramer-Zucker, A.G. *et al.* Cilia-driven fluid flow in the zebrafish pronephros, brain and Kupffer's vesicle is required for normal organogenesis. *Development* **132**, 1907-1921 (2005).

74. Gan, B. *et al.* Role of FIP200 in cardiac and liver development and its regulation of TNFalpha and TSC-mTOR signaling pathways. *J Cell Biol* **175**, 121-133 (2006).

75. Sou, Y.S. *et al.* The Atg8 conjugation system is indispensable for proper development of autophagic isolation membranes in mice. *Mol Biol Cell* **19**, 4762-4775 (2008).

76. Kaizuka, T. *et al.* An Autophagic Flux Probe that Releases an Internal Control. *Mol Cell* **64**, 835-849 (2016).

77. Saitoh, T., Nakano, H., Yamamoto, N. & Yamaoka, S. Lymphotoxin-beta receptor mediates NEMO-independent NF-kappaB activation. *FEBS Lett* **532**, 45-51 (2002).

78. Morita, K. *et al.* Genome-wide CRISPR screen identifies TMEM41B as a gene required for autophagosome formation. *J Cell Biol* **217**, 3817-3828 (2018).

79. Hosokawa, N., Hara, Y. & Mizushima, N. Generation of cell lines with tetracycline-regulated autophagy and a role for autophagy in controlling cell size. *FEBS Lett* **580**, 2623-2629 (2006).

80. Dummer, A., Poelma, C., DeRuiter, M.C., Goumans, M.J. & Hierck, B.P. Measuring the primary cilium length: improved method for unbiased high-throughput analysis. *Cilia* **5**, 7 (2016).

81. Schwanhausser, B. *et al.* Global quantification of mammalian gene expression control. *Nature* **473**, 337-342 (2011).

82. Masuda, T., Tomita, M. & Ishihama, Y. Phase transfer surfactant-aided trypsin digestion for membrane proteome analysis. *J Proteome Res* **7**, 731-740 (2008).

83. Rappsilber, J., Mann, M. & Ishihama, Y. Protocol for micro-purification, enrichment, pre-fractionation and storage of peptides for proteomics using StageTips. *Nat Protoc* **2**, 1896-1906 (2007).

84. Boersema, P.J., Raijmakers, R., Lemeer, S., Mohammed, S. & Heck, A.J. Multiplex peptide stable isotope dimethyl labeling for quantitative proteomics. *Nat Protoc* **4**, 484-494 (2009).

85. Kumar, S., Stecher, G., Li, M., Knyaz, C. & Tamura, K. MEGA X: Molecular Evolutionary Genetics Analysis across Computing Platforms. *Mol Biol Evol* **35**, 1547-1549 (2018).

86. Singh, N., and Bhalla, N. Moonlighting Proteins. *Annu Rev Genet* **54**, 265-285 (2020)

87. Minoshima, Y., *et al.* Phosphorylation by aurora B converts MgcRacGAP to a RhoGAP during cytokinesis. *Dev Cell* **4**, 549-560 (2003).

Acknowledgments

I thank Professor Takahide Nagase for his mentorship and encouragement, Professor Noboru Mizushima for showing me what a researcher is and how fascinating research can be. I appreciate Haruka Chino for teaching me the basics of how to perform experiments from scratch, Hayashi Yamamoto for constructive discussion, Saori Yoshii for mouse sampling, Keiko Igarashi for help with histological examinations, Shoji Yamaoka for pMRX-vector, Teruhito Yasui for pCG-VSV-G and pCG-gag-pol, Robert A. Weinberg for pCMV-VSV-G, Didier Trono for psPAX2, and Keith Mostov for pLKO.1-blast vector.

I would like to thank all lab members for helping me. Finally, I would like to express my sincere gratitude to my wife and my two wonderful children for supporting me throughout my research life.